Additively Manufactured 17-4 PH Stainless Steels for Fracture Management Devices

Aruntapan Dash, Susmita Bose, and Amit Bandyopadhyay*

W. M. Keck Biomedical Materials Research LaboratorySchool of Mechanical and Materials EngineeringWashington State University, Pullman, Washington, 99164, USA.

*Corresponding author email – <u>amitband@wsu.edu</u>

Abstract

Stainless steel 316L (SS316L) is widely used in fracture management devices. However, SS316L does not offer any bacterial infection resistance and can cause metal-ion sensitivity due to Ni-ions' presence. 17-4PH can emerge as a promising substitute due to the intrinsic antibacterial properties of copper, a 75% reduction in nickel content, and superior mechanical properties. SS316L and 17-4 PH were manufactured using laser-directed energy deposition (LDED). 17-4PH specimens surpassed the compressive strength of SS316L by over 150%. A static magnetic field was generated in 17-4 PH specimens to understand *in vitro* bone cell-material interactions. *In vitro* human fetal osteoblast cell culture and bacterial inhibition study using *Staphylococcus aureus* and *Pseudomonas aeruginosa* were carried out on these specimens with SS316L as control and as-processed and magnetized 17-4 PH as treatments. Results demonstrated that magnetized 17-4 PH exhibited 25% enhancement in hFOB proliferation and 70% reduction in bacterial colonization compared to SS316L.

Keywords: 17-4PH; Additive manufacturing; 3D printing; hFOB cell culture; Staphylococcus aureus (S. aureus); Pseudomonas aeruginosa (P. aeruginosa).

1 Introduction

More than 50 million road traffic accidents (RTAs) occur yearly, causing casualties and disabilities, as published by the World Health Organization (WHO). Since most RTAs occur in remote locations, the injuries are highly susceptible to infection due to the exposure of open wounds for a prolonged duration [1], [2]. Notably, bacterial infections such as osteomyelitis are one of the most lethal reasons for fatalities, with a mortality rate of ~24% and ~50% among patients with ages ≥ 65 and ≥ 85 , respectively [3]. Osteoporosis and osteoarthritis are also prominent contributors to chronic disease morbidity, with osteoporotic fractures impacting over 8.9 million individuals and osteoarthritis affecting 58.5 million people in the United States alone [4]. Globally, more than 178 million individuals are affected by fractures associated with osteoporosis and osteoarthritis [5]. The increasing demand for orthopedic implants is thus expected to witness exponential growth [3], [6]. Projections indicate that the global orthopedic implant market will grow from 128 billion in 2023 to 144 billion in 2024 at a compound annual growth rate (CAGR) of 12.6% and is poised to reach a business value of \$218 billion by 2028 at a CAGR of 10.9% [7]. It is imperative to innovate suitable orthopedic implants to meet the burgeoning demand.

Throughout historical observations, elemental iron (Fe) has consistently manifested its non-adverse engagement with human physiology. Stainless steels are widely used in various biomedical applications [8]. Among different grades of stainless steel, 316L (SS316L) has had the maximum number of biomedical applications, starting from fracture fixation to total arthroplasty [9]. While the cost-effectiveness and robust corrosion resistance rendered austenitic SS316L a material for biomedical applications, its predominant drawback as an implant material lies with poor biocompatibility, high stiffness, and a lack of antibacterial resistance fostering microbial-induced implant failure [10]. Infection of the implant surface can ultimately lead to severe health complications such as inflammation, amputation, and even mortality [11]. Staphylococcus aureus (S. aureus) and Pseudomonas aeruginosa (P. aeruginosa) are the two most common bacterial strains accounting for infections at the orthopedic, spinal, and dental implant sites [12].

SS316L is a Chromium (Cr)-Nickel (Ni) steel with ~17% Cr and ~12% Ni as the major alloying elements. Recent investigations have explored metal ion sensitivity, categorizing the

elements in descending order of harmful potential as follows: cobalt > vanadium > nickel > chromium > titanium > iron [8]. A high percentage of Ni in the physiological environment can be potentially toxic [13] and lead to dermatitis, chronic rhinitis, and cancer-causing genetic mutations [8]. It has been reported that SS316L metallic implants are prone to releasing Ni ions when exposed to body fluids for an extended period and are the leading cause of metal ion sensitivity [14]. An investigation is justified for an alternate implant material with inherent antibacterial resistance and minimal metal ion sensitivity without compromising mechanical properties. 17-4 PH is Cr-Ni stainless steel with an equivalent percentage of Cr and ~75% less Ni than the SS316L. The mechanical attributes of 17-4 PH stainless steel are derived from the precipitation of inherent copper particles [15]. Copper (Cu) possesses well-documented antibacterial and infection-preventive properties [12]. Researchers discovered that superior antibacterial activity associated with 17-4 PH is primarily due to the copper-rich precipitate that results from a saturated quantity of copper in the steel matrix following an aging treatment [16]. There may be a likelihood of a chemical reaction between the copper-rich precipitation and the stainless-steel matrix. This reaction will destroy bacterial cell membranes and walls, further change cell permeability, and ultimately result in bacterial death [17]. It is hypothesized that Cu and the reduced Ni in 17-4 PH will allow bacterial inhibition and minimization of the Ni-ion sensitivity, respectively.

Among different metal additive manufacturing (AM) techniques [18], laser-directed energy deposition (LDED) emerges prominently among the seven ASTM-classified AM processes capable of depositing both powder and wire feedstock materials melted by a laser [19], [20]. The progression of LDED technology has led to the proliferation of location- and application-specific structures across diverse industries such as energy, automotive, aerospace, nuclear, transport, and biomedical [21], [22], [23], [24]. Today, AM stands as a revolutionary approach that evolved from the prototyping phase to an era of manufacturing on-demand, patient-specific, and highly customized functional implants. Hence, the present investigation employed additively manufactured SS316L and 17-4 PH specimens for the analysis.

The therapeutic effects associated with the magnetic field are expected to have noninvasive healing properties for both hard and soft tissues. Researchers have claimed higher cellular turnover rates upon applying static magnetic fields (SMF) in orthodontic applications

[25]. SMFs have already been acknowledged as a supplementary medicine tool because they control specific cell metabolism and enhance regeneration [26], [27]. Researchers have produced various findings on the bioeffects of cells associated with SMFs, both *in vitro* and *in vivo*, which claim to promote cell migration, proliferation, and differentiation [28], [29]. Although numerous experiments have been performed to understand the influence of magnetization on the growth, proliferation, and differentiation of human tissue and cells [30], results have been contradictory and have not yet been wholly explained [31], [32]. To this date, several biological studies have been conducted in different species of animals and cell cultures, but little is known about the biological effects of magnets on humans at this time [33], and there is still debate about the biophysical rationale for their usage [34].

The present investigation addresses a fundamental question: can we use 17-4 PH stainless steel as an alternative to SS316L in fracture management-related load-bearing implants? We employed the LDED technique [20], [35] to fabricate specimens of SS316L and 17-4 PH. Comprehensive assessments were performed to appraise their mechanical properties, including microhardness measurements and quasistatic compression tests. Detailed phase and microstructural analyses were done to understand their influence on mechanical properties. A set of 17-4 PH samples were magnetized. In vitro tests were done using human fetal osteoblast (hFOB) cells utilizing 3D printed SS316L as control, as-processed and magnetized 17-4 PH as treatments to investigate the influence of induced magnetism cell proliferation. In vitro studies were carried out on both control and treatment samples using S. aureus and P. aeruginosa strains to understand the impact of copper on bacterial inhibition.

2 Materials and methods

2.1 Laser-directed energy deposition (LDED) of SS316L and 17-4 PH

17-4 PH powders (Carpenter Tech. Corp., PA) with a mean particle size ranging from 15 to 53 μm and SS316L powders (Höganäs, Sweden) between 53 and 150 μm were used. Both powders used in the current research are gas-atomized and spherical. Supplementary **Table ST 1** provides a detailed breakdown of the elemental composition present in the starting powders.

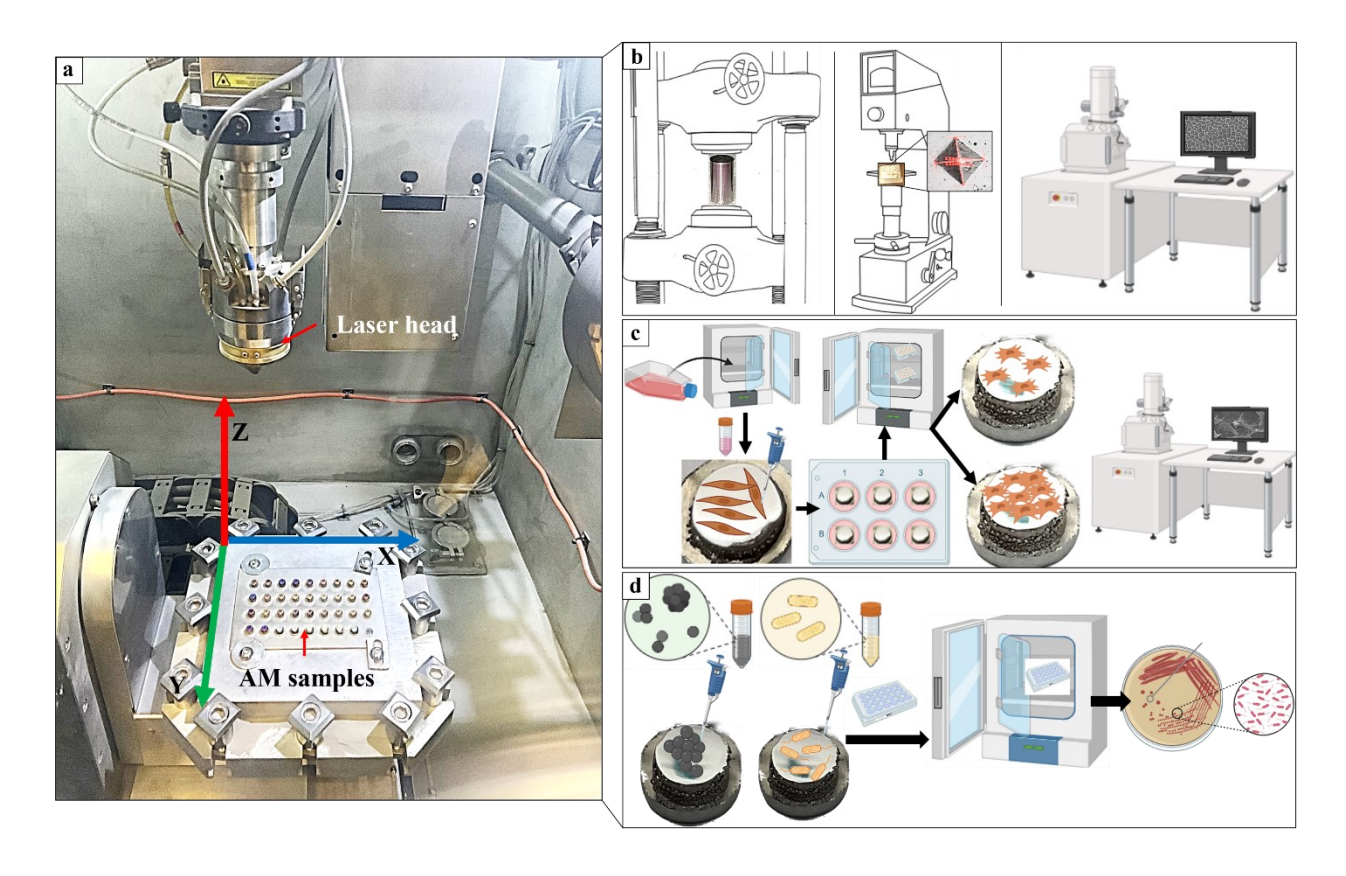


Figure 1: (a) Laser-directed energy deposition (LDED) system for fabrication of SS316L and 17-4 PH stainless steels; (b) schematics of mechanical testing and microstructural analysis of the AMed samples, (c) schematics of *in vitro* hFOB cell culture, (d) schematics of *S. aureus* and *P. aeruginosa* bacterial culture on the additively manufactured samples.

A laser-directed energy deposition (LDED) [36] setup, FormAlloy (Spring Valley, CA), equipped with twin powder feeders and a 1-kW fiber laser, was employed to produce both SS316L and 17-4 PH compositions. This LDED setup features an actively cooled build platform with movement capabilities along the X and Y coordinates. The 1 kW laser source is placed on the Z-spindle normal to the build platform, as shown in **Fig. 1a**. To prevent oxidation, the LDED setup operates within an inert (Ar) environment, ensuring the O₂ levels remain below 20 ppm. The continuous fiber laser beam, with power reaching up to 1 kW, is used to melt deposited powders onto a substrate.

To print the desired structures of SS316L and 17-4 PH, computer-aided design (CAD) files containing the necessary dimensions were imported into the computer-aided manufacturing

(CAM) software to generate the required toolpath. Considering potential defects like lack of fusion, porosity, and keyhole defects that could significantly impact the mechanical properties and pose risks to the reliability of the printed components [35], a series of AM experiments were conducted before the final printing stage. These experiments were conducted to determine the optimal and refined processing parameters before the final printing step. **Table 1** presents the comprehensive optimal print parameters for both compositions. This table also illustrates the volumetric energy density (Ev), representing the energy supplied by the laser power source to the powder volume [35]. This relationship is expressed by the equation provided below.

$$E_v = \frac{P}{v.\,h.\,t} \tag{1}$$

In the context of the equation, v denotes the scanning speed (mm/s), h represents the hatch spacing (mm), maintaining a consistent value of 0.5 for all samples, t corresponds to the layer thickness (mm), and P signifies the laser power in (W).

Table 1: Optimized process parameters and compositional nomenclature of the samples manufactured through powder-based LDED process.

Samples		Laser power		Speed			Gas flow rate (liters/min)		Powder	
		(Watt)		(mm/min)					feeder	
Sample composition	Sample ID	Infill power	Contour	Infill speed	Contour	Layer thickness (mm)	Shield gas	Carrier gas	Disc rate (rpm)	Volumetric energy density (J/mm³)
Pure SS316L	S_1	350	350	800	800	0.3	13	9	0.6	175
Pure 17-4 PH	S_2	400	400	1200	1200				0.5	133

2.2 Microstructural characterization and phase analysis

Specimens measuring 10 mm x 10 mm x 8 mm were processed for microstructural characterization and phase analysis. The SS316L and 17-4 PH printed samples were subjected to longitudinal cutting with a low-velocity diamond saw. Subsequently, they were ground with silicon carbide (SiC) papers ranging from 80 to 2000 grit sizes and polished for 15 minutes each using a suspension of 1-0.05 μ m Al₂O₃/DI water. Etching followed, involving submersion in a solution composed of 10 ml HNO₃, 15 ml HCl, 10 ml CH₃COOH, and 2-5 drops of glycerol [37] for 30 – 45 seconds. In order to investigate macro and microstructures, the etched metallographic samples were analyzed at different magnifications using a digital optical microscope (Keyence VHX 7000 series) and a field-emission scanning electron microscopy (SEM, Apreo VolumescopeTM, Thermo Fisher Scientific, Waltham, MA). Phase analysis of the mirrorpolished surfaces of SS316L and 17-4 PH specimens was done using a Rigaku mini flex 600 X-ray diffractometer. Equipped with a 2-D General Area Diffraction Detector (GADDS) on a θ - θ goniometer, the diffractometer scanned the samples using Cu- k_{α} radiation (1.54 Å at 40 kV and 20 mA) at a speed of 5° per minute within the range of 35° \leq 20 \leq 100°.

2.3 Microhardness and compression testing

Cylindrical specimens of SS316L and 17-4 PH, featuring an 8 mm diameter and 15 mm height, were printed for compressive strength testing. According to the ASTM standard E92-23 [38], Vicker's cross-sectional hardness profile in the build direction of the samples, spanning from the bottom zone to the top zone, was obtained employing a Phase II Plus Micro Vickers hardness tester (Upper Saddle River, NJ, USA). A load of 1.961 N (HV_{0.2}) was applied for a dwell period of 15s. Approximately 20–30 indents were taken in each zone. The cylindrical compression specimens were further milled to a final diameter of 7 mm and then turned the cross-sectional area to a final gauge length of 14 mm, which is per ISO/ ASTM E9-19 standard [39] using a 3-axis CNC mill-turn setup. The specimens were subjected to quasistatic compression testing utilizing the Instron servo-hydraulic universal testing machine (135 kN load cell) at ambient temperature, employing a 0.1 mm/min crosshead displacement rate. The applied load for all samples was aligned parallel to the build direction. At least three replicates from each

composition underwent compression testing under an ambient temperature and quasistatic environment to ensure statistical significance. The schematics of the mechanical testing and microstructure analysis of the printed samples are shown in **Fig. 1b**.

2.4 In vitro study and magnetization of the 17-4 PH specimens

For *in vitro* human fetal osteoblast (hFOB) cell culture and bacterial inhibition study, specific disc specimens of SS316L and 17-4 PH with 8 mm diameter and ~4.5mm height were printed. The *in vitro* samples were cut along with the build plate using an abrasive water jet machine (WAZER Inc., USA) and polished using 80-2000 grit size SiC papers to prepare them for the study. Faraday's law of electromagnetic induction states that a moving charge (current) generates a magnetic field. The principle of electromagnetic induction magnetized the 17-4 PH samples. The setup is shown in supplementary **Fig. S1.** A DC power source of 20V is used to deliver the desired amount of current for inducing magnetism in the AM'ed 17-4 PH samples. The 17-4 PH stainless steel sample was wound using a 21 AWG magnet wire. The two ends of the wire were then connected to the positive and negative terminals of the power source for 5s. The average value of induced magnetism in the 17-4 PH samples was 168±13 μT. These magnetic specimens were used as treatment samples to understand the effect of the magnetic field on the hFOB proliferation.

The specimens were subjected to *in vitro* analysis to study bone-cell materials interaction with human fetal osteoblast (hFOB cell line1.19) (ATCC, Manassas, VA, USA) cells [40] for 3 and 7 days. The schematics of the *in vitro* hFOB cell culture are shown in **Fig. 1c**. SS316L served as the control (C), while the samples designated as as-processed 17-4 PH (T₁) and magnetized 17-4 PH (T₂) were considered as treatments. The disc specimens underwent sterilization via autoclaving at 121°C for 1h. Following sterilization, 25x10³ cells were seeded per well onto the smooth surface of the printed samples, which were subsequently positioned in 24 well plates. A fusion of Ham's F12 Medium and Dulbecco's Modified Eagle's Medium (DMEM/F12, Sigma, St. Louis, MO) was utilized at a 1:1 proportion, including 2.5 mM L-glutamine (lacking phenol red), as the growth medium. This medium was fortified with 10% fetal bovine serum (ATCC, Manassas, VA) and supplemented with 0.3 mg/ml G418 sulfate salt

(Sigma). Cultures were maintained at 34 °C in an incubator with 5% CO₂, and the cell media were refreshed every 2 days throughout the experimental period.

The proliferation of viable hFOB cells on AM'ed samples was assessed using the MTT assay. The MTT (3-(4, 5-dimethylthiazol-2-yl)-2, 5-diphenyl tetrazolium bromide) assay was conducted at two-time points, 3- and 7-days post-incubation [40], [41]. A solution of MTT (Sigma) salt at 5mg/ml concentration in phosphate buffer saline (PBS) was prepared and sterilized using a 0.2 μm pore filter sterilization unit. Subsequently, 100 μl of the MTT solution was mixed with 900 μl of DMEM culture media supplemented with 10% fetal bovine serum and added to each sample to initiate formazan crystal formation catalyzed by mitochondrial dehydrogenases. After incubation at 34 °C for 2 h, the samples were transferred to a new 24-well plate. Formazan crystals were dissolved using a solubilization solution containing 10% Triton X-100, 0.1 N HCl, and isopropanol (1 ml). Then, 100 μl of the resulting supernatant was transferred to a 96-well plate, generating 3 data points per specimen. The optical density of the solution in each well was measured at a wavelength of 570 nanometers using a microplate reader (Cambridge Tech., MA, USA).

To evaluate the cellular structure of the cultured specimens via FESEM, a fixation solution composed of 2% paraformaldehyde/ 2% glutaraldehyde in 0.1 M phosphate buffer was employed to fix the samples overnight at 4 °C. After fixation, the specimens underwent triple rinsing with PBS buffer to remove any residual fixative, after which 2% osmium tetroxide (OsO₄) was introduced and allowed to react for 2 hours at ambient temperature. Serial dehydration of the fixed specimens was performed using ethanol (30%, 50%, 70%, 95%, and thrice with 100%), followed by critical drying using hexamethyldisilane (HMDS) [40], [41]. The samples were gold-coated before FESEM imaging.

2.5 In vitro bacterial cell culture

The *in vitro* bacterial culture was carried out on the polished surface of the SS316L (C), 17-4 PH (T₁), and magnetized 17-4 PH (T₂) according to the modified ISO 22196:2011 standard [42]. **Fig. 1d** illustrates the schematics of the *in vitro* bacterial culture executed using *S. aureus* (gram-positive) and *P. aeruginosa* (gram-negative) bacterial strains. The bacterial culture was

conducted for both bacterial strains over 24 h and 72 h. Freeze-dried S. aureus (Carolina Biological, NC, USA) and P. aeruginosa were rehydrated using rehydration media followed by subsequent dilutions for 0.5 McFarland standard optical density measurement to identify the correct dilution of 1.5 x 10⁸ colony forming units (CFU) per ml. The polished disc specimens were first sterilized by autoclaving at 121°C for one hour; then, the sterile specimens were placed in 24 well plates. Triplicates of each specimen were taken to count the bacterial colony formed over the agar plate. In contrast, duplicates of each specimen were taken to analyze the bacterial cell morphology via SEM. In a 24-well plate, specimens were positioned individually, and 10⁶ CFU of bacterial colonies were introduced onto the sterile polished surfaces, supplemented with 2 ml of nutrient broth per well. At designated time intervals, bacterial cells were scraped from the surfaces of three out of five specimens using cell scrapers. These cells were then mixed in 2 ml of 0.1 M phosphate buffer saline and subjected to serial dilution, aiming to yield solutions with colonies ranging between 10 and 100 CFU in 10 μl. Subsequently, ten μl of the respective solutions were streaked on a tryptic soy agar plate (Nutrient agar, Hardy Diagnostic, CA, USA) for S. aureus and cetrimide agar plate (Pseudosel agar, Fisher Scientific, NH) for P. aeruginosa. The count of bacterial colonies on agar plates was conducted after 24 h of incubation at 37 °C. The antibacterial efficacy was calculated based on the number of bacterial colonies (N) present on individual material compositions and was calculated using open-source image processing(GIMP 2.10.32) software [43], [44]. The equation below expresses the antibacterial resistance (R) (in %).

$$R = \frac{N_{control} - N_{treatment}}{N_{control}} \times 100$$
 ...(2)

After the respective time points, the duplicate specimens dedicated for bacterial cell morphology evaluation were preserved by putting 2 ml of the fixative solution followed by serial dehydration, as described in **section 2.4**. These specimens were gold-coated and imaged under FESEM for cell morphology analysis.

2.6 Statistical Analysis

The data from multiple experiments are presented as the average \pm standard deviation, visually represented through error bars. Statistical analyses were executed employing a 1-way analysis of variance using Minitab software (Minitab, LLC, PA). Tukey-Kramer simulations were conducted to facilitate pairwise comparisons of means among treatments, with a significance level (α) set at 0.05. Statistical significance was denoted by a p-value $< \alpha$. Comprehensive analysis of variance tables for all treatments and respective p-value comparison tables for Tukey-Kramer models are given in the supplemental document **Supp 1.docx**.

3 Results

Microstructural characterizations of additively manufactured SS316L and 17-4 PH using optical and scanning electron microscopy (SEM) and phase analysis are shown in **Fig. 2**. Mechanical properties, including microhardness profile and quasistatic compression testing, are shown in **Fig. 3**. **Fig. 4** shows findings from the MTT assay of hFOB cells after 3 and 7 days of culture. *In vitro*, bacterial cell culture results, including agar plate count and the bacterial cell morphology evaluation for *S. aureus* and *P. aeruginosa*, are presented in **Figs. 5** to **8**.

3.1 Microstructural characterization and phase analysis

The additively manufactured SS316L surface image in **Fig. 2a** demonstrates the robust build quality. This is further evidenced by the high-definition optical image (**Fig. 2a**₁) at higher magnification, showing the build devoid of unmelted powder particles and defects. The SEM micrographs of the SS316L show variation and can be classified into cellular (**Fig. 2a**₂), columnar dendritic (**Fig. 2a**₃), and dendritic (**Fig. 2a**₄). The low-magnification stereoscope image (**Fig. 2b**) of the 17-4 PH also showed a build devoid of defects. The high-magnification optical image (**Fig. 2b**₁) also supports this, showing the initial layers without any remaining unmelted powder particles. The primary microstructure of 17-4 PH was confirmed to be lathy martensite from the images (**Fig. 2b**₂, **b**₃). Vunnam et al. [30] and Dash et al. [38] also reported a similar microstructural evolution.

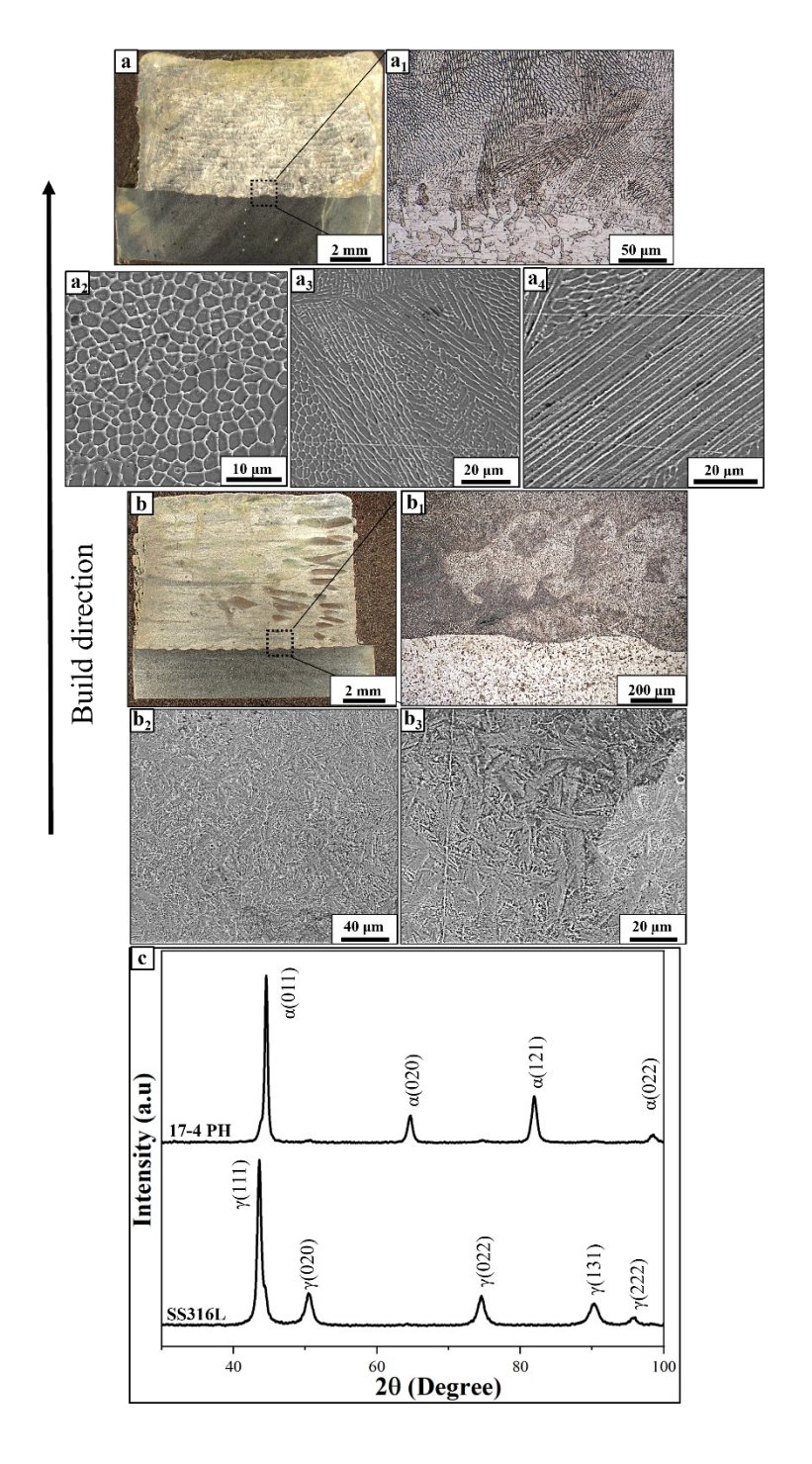


Figure 2: (a) Stereoscope image of AMed SS316L, (a₁) Macrostructure at high magnification displaying the flawless interface between the printed SS316L and substrate, free of any defects or unmelted particles, (a₂, a₃) cellular and columnar dendritic microstructure present in the SS316L print, (a₄) dendritic microstructure of the SS316L, (b) stereoscope image of AMed 17-4 PH, (b₁) digital optical image at low magnification displaying the pristine interface between the

substrate and the printed 17-4 PH with no unmelted particles, (b₂, b₃) SEM micrographs of the AMed 17-4 PH at low and high magnification, (c) X-ray diffractograms of 3D printed bulk SS316L and 17-4 PH with scanning direction along the build direction.

Fig. 2c shows the X-ray diffraction patterns of both specimens, with the scan direction aligned with the build direction. For SS316L, the predominant phase was identified as face-centered cubic (FCC) γ (JCPDS 96-900-8470), with a preferred orientation along the (111) plane at 2θ of 43.63°. Similar trends have been reported by Dash et al. [35]. For the bulk 17-4 PH specimens, the dominant phase was body-centered cubic (BCC) α (JCPDS 96-901-3475), with a favored orientation along the (011) plane at 44.62° of 2θ. The γ phase is absent in 17-4 PH. SEM micrographs in **Fig. 2b2** and **b3** for 17-4 PH showed martensitic microstructure. Introducing a delay period between consecutive layers during the 17-4 PH printing process could be a potential reason for this phase formation [35]. The bulk specimens show peak broadening and a positive peak shift compared to their powder counterparts.

3.2 Microhardness and compression testing

Vickers microhardness tests were carried out on the polished surface of bulk SS316L and 17-4 PH specimens. The measurements were initiated from the initial layer and were taken at 0.5 mm intervals along the build direction. Three hardness measurements were obtained, two at the edges and one at the center along each print direction, shown in Supplementary Fig. S2. Such measurements were taken from the first to the final printed layer. The resulting hardness values and their standard deviation have been presented in Fig. 3a. The mean microhardness value for SS316L and 17-4 PH was $220 \pm 9 \text{ HV}_{0.2}$ and $303 \pm 9 \text{ HV}_{0.2}$, respectively. Cu-rich clusters and NbC particles could account for the increased hardness observed in the 17-4 PH samples [45]. It can be visualized from Fig. 3a that the hardness profile for the SS316L showed a reducing trend from the first layer to the final layer; however, the same was less pronounced for the 17-4 PH.

Fig. 3b presents the stress vs. strain plots and the post-compression microstructures for SS316L and 17-4 PH. The 0.2% offset yield strength under un-axial compression for the SS316L and 17-4 PH was measured to be 356 ± 17 MPa and 914 ± 8 MPa, respectively. The 0.2% offset

yield strength for the AMed 17-4 PH showed lower numbers than the conventional counterparts under the H900 condition [46]. The 0.2% offset yield strength for the AMed SS316L showed elevated numbers than that of the wrought counterparts [47]. A linear strain hardening phenomenon can be seen in the plastic deformation zone for SS316L. However, a constant plastic deformation zone is observed in the case of 17-4 PH, possibly due to the presence of isotropic lath martensitic microstructure. Post-compression SEM micrographs of the 17-4 PH and SS316L showed the cracks and presence of slip lines in **Fig. 3b**₁ and **b**₂, respectively.

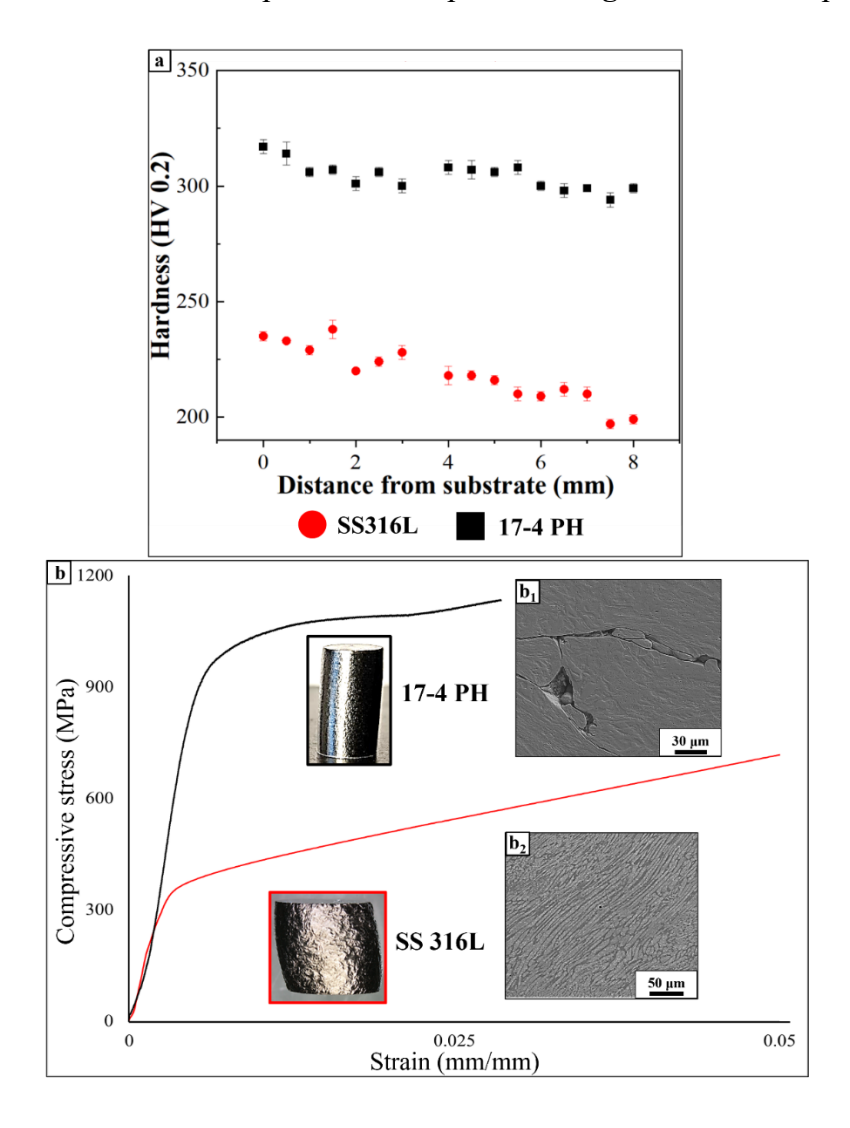


Figure 3: (a) Vicker's microhardness profile, (b) representative stress vs. strain curve of AMed SS316L and 17-4 PH samples (Insert images taken after compression testing is done), (b₁) SEM image showing cracks post-compression in the microstructure of 17-4 PH, (b₂) SEM image showing the flow of grains post compression in the microstructure of SS316L.

3.3 *In vitro* hFOB cell culture

An MTT assay and morphological study using SEM have been carried out on the surface of AMed SS316L (C), 17-4 PH (T1), and magnetized 17-4 PH (T2) to understand the effect of static magnetism on cellular proliferation. The MTT assay was used to quantitatively determine the proliferation of viable hFOB cells on the surfaces of SS316L and 17-4 PH. **Fig. 4a** compares viable cell densities for different specimens after 3 and 7 days of incubation. Cells proliferated better on the 17-4 PH magnetized specimens for the culture duration than the SS316L. The differences in optical density (OD) were almost 24.5% higher on the magnetized 17-4 PH specimens than the SS316L control surfaces after 7 days of culture. However, there is only a 7% increase in OD value on as-processed 17-4 PH than SS316L control after 7 days of culture. No cytotoxicity can be seen due to the presence of copper in the 17-4 PH specimens. Statistical analysis revealed that a significant difference (p < 0.05) and an extremely high significant difference (p < 0.01) in optical density were present between the 17-4 PH and SS316L specimens and magnetized 17-4 PH and SS316L specimens, respectively.

Cell morphology was observed after 3 and 7 days of incubation by FESEM. The FESEM observation showed the attachment, growth, and proliferation of the hFOB cells. **Fig. 4b** revealed the cell morphologies after 3 and 7 days of incubation. Cells were observed to adhere to each other with a filopodial extension on the surfaces of both as-processed and magnetized 17-4 PH specimens after 3 days. However, limited growth and proliferation of the cells were observed with an under-developed filopodial extension on the surface of the SS316L specimen after 3 days. However, after 7 days, the surfaces of both as-processed and magnetized 17-4 PH specimens were covered with cells having an abundant amount of filopodial extensions, **Fig. 4b**. On the smooth surface of as-processed and magnetized 17-4 PH, cells displayed a flat, evenly dispersed appearance and developed in a monolayer. However, the growth of the cells was not prominent on the control SS16L surface, **Fig. 4b**. It was observed that the cells formed multilayer clusters on the smooth surface of the magnetized 17-4 PH sample, implying better cell attachment and proliferation.

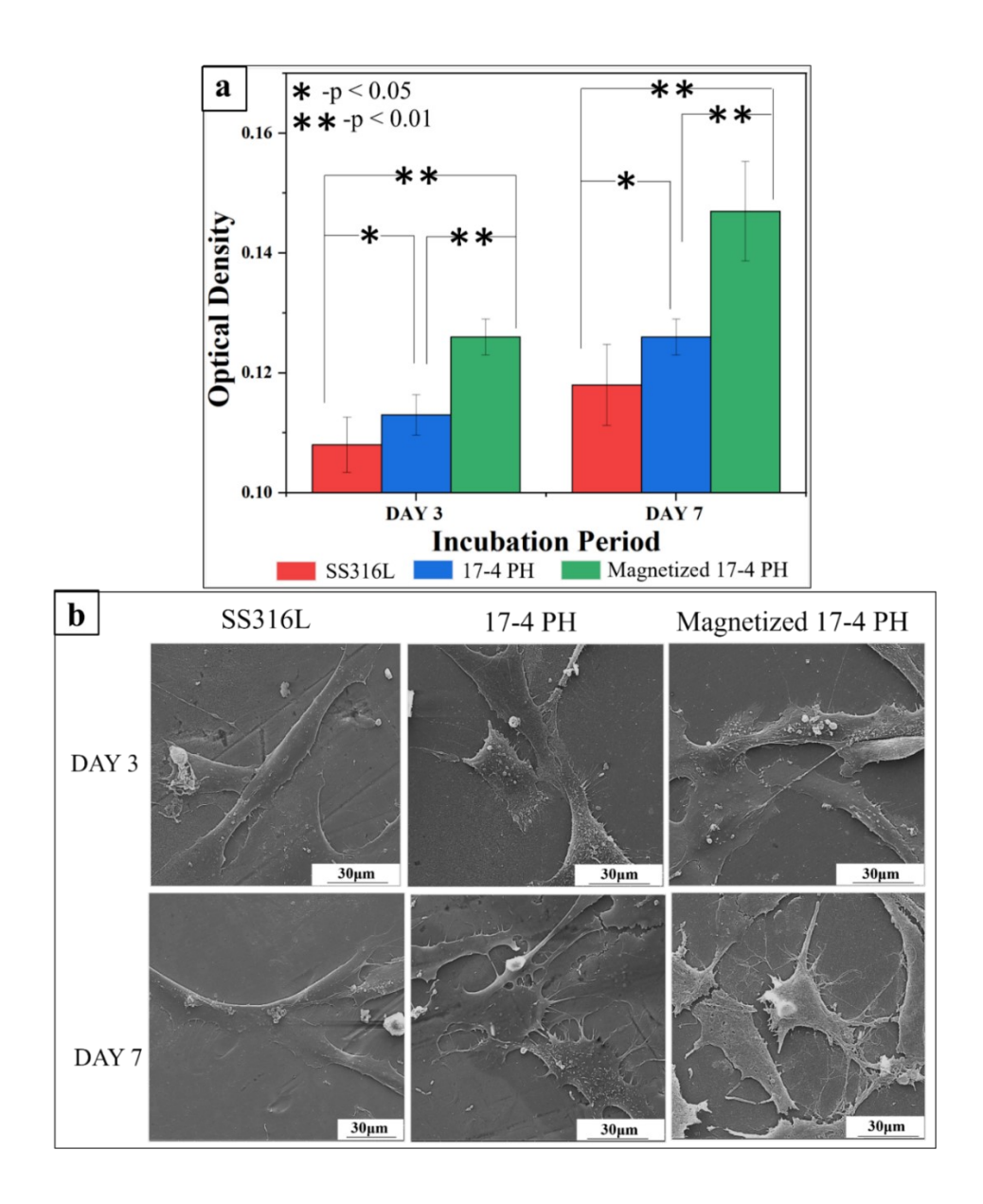


Figure 4: (a) The MTT assay was performed on hFOB cells incubated for 3 and 7 days on control samples (SS316L) and treatment samples (17-4 PH and magnetized 17-4 PH). Statistical analyses were conducted using a one-way analysis of variance for a sample size (n) of 3 and a p-value of 0.05. Statistical significance was determined through pairwise assessment of means between control and treatments and among treatments. Results with p < 0.05 were considered significantly different and marked with '*', while those with p < 0.01 were regarded as exceptionally statistically significant and denoted by '**'; (b) SEM micrographs showing osteoblast proliferation at day three and day seven incubation periods for control (SS316L) and treatment samples (17-4 PH and magnetized 17-4PH).

3.4 In vitro gram-positive S. aureus bacterial culture

With 3 - 5% copper content, a well-known antibacterial agent, 17-4 PH can potentially thwart bacterial infections at the implant site. In order to validate this, the bacterial activity employing a gram-positive S. aureus strain underwent an investigation for 24 and 72 h. The quantification of viable S. aureus colonies for each composition is shown in the bar chart, Fig. 5a. 17-4 PH exhibited an antibacterial efficacy of 58% and 71% against the S. aureus after 24 and 72 h, respectively (Fig. 5b). Magnetized 17-4 PH demonstrated antibacterial efficacy of 42 and 60% against S. aureus after 24 and 72 h, respectively (Fig. 5b). Morphological analysis of S. aureus exhibited increased bacterial growth on the surface of SS316L control from 24 to 72 h. This enhancement was corroborated by ultra-high-resolution SEM images showing healthy bacterial colonies. However, the treatment specimens, as-processed and magnetized 17-4 PH, demonstrated a decline in bacterial colony growth over the same period. The SEM micrographs revealed septum formation for magnetized 17-4 PH as early as 24 h, while as-processed 17-4 PH exhibited complete cytoplasm dilation within 72 h of surface exposure. SEM micrographs unveiled septum formation for magnetized 17-4 PH as early as 24 h, whereas 17-4 PH displayed complete cytoplasm dilation within 72 h of exposure. The 17-4 PH compositions minimized bacterial growth for up to 72 h, Fig. 6.

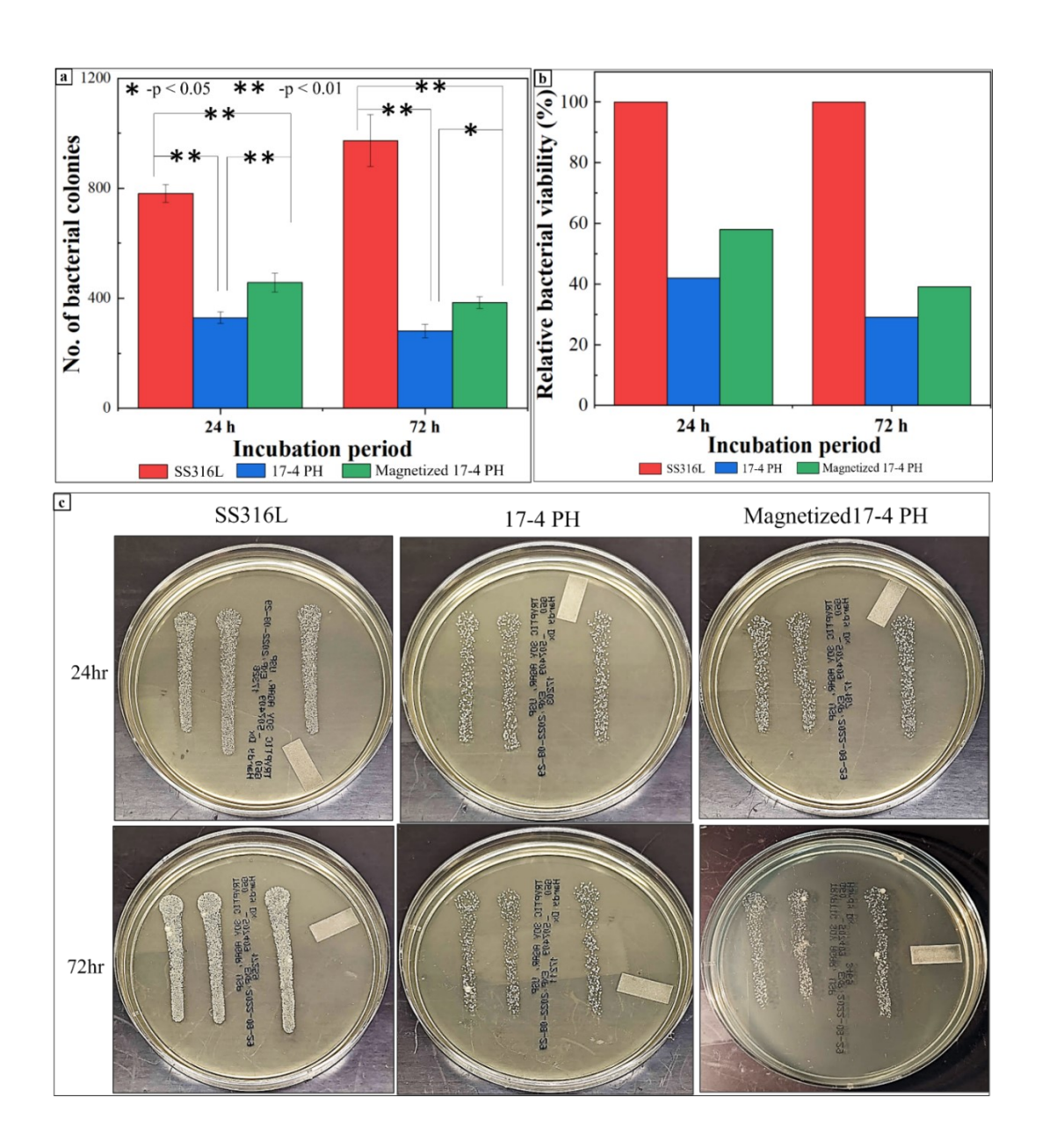


Figure 5: Results from the *in vitro* bacterial inhibition experiment against *S. aureus*. (a) quantitative representation of the number of CFUs after 24 and 72 h culture of the *S. aureus* bacterial strain. Statistical analyses were conducted using a one-way analysis of variance for a sample size (n) of 3 and a p-value of 0.05. Statistical significance was determined through pairwise assessment of means between control and treatments and among treatments. Results with p < 0.05 were considered significantly different and marked with '*', while those with p < 0.01 were regarded as extremely significant and denoted by '**'; (b) plot showing relative bacterial viability after 24 and 72 h culture, (c) high-definition agar plate images showing the CFU formation for *S. aureus* for 24 and 72h.

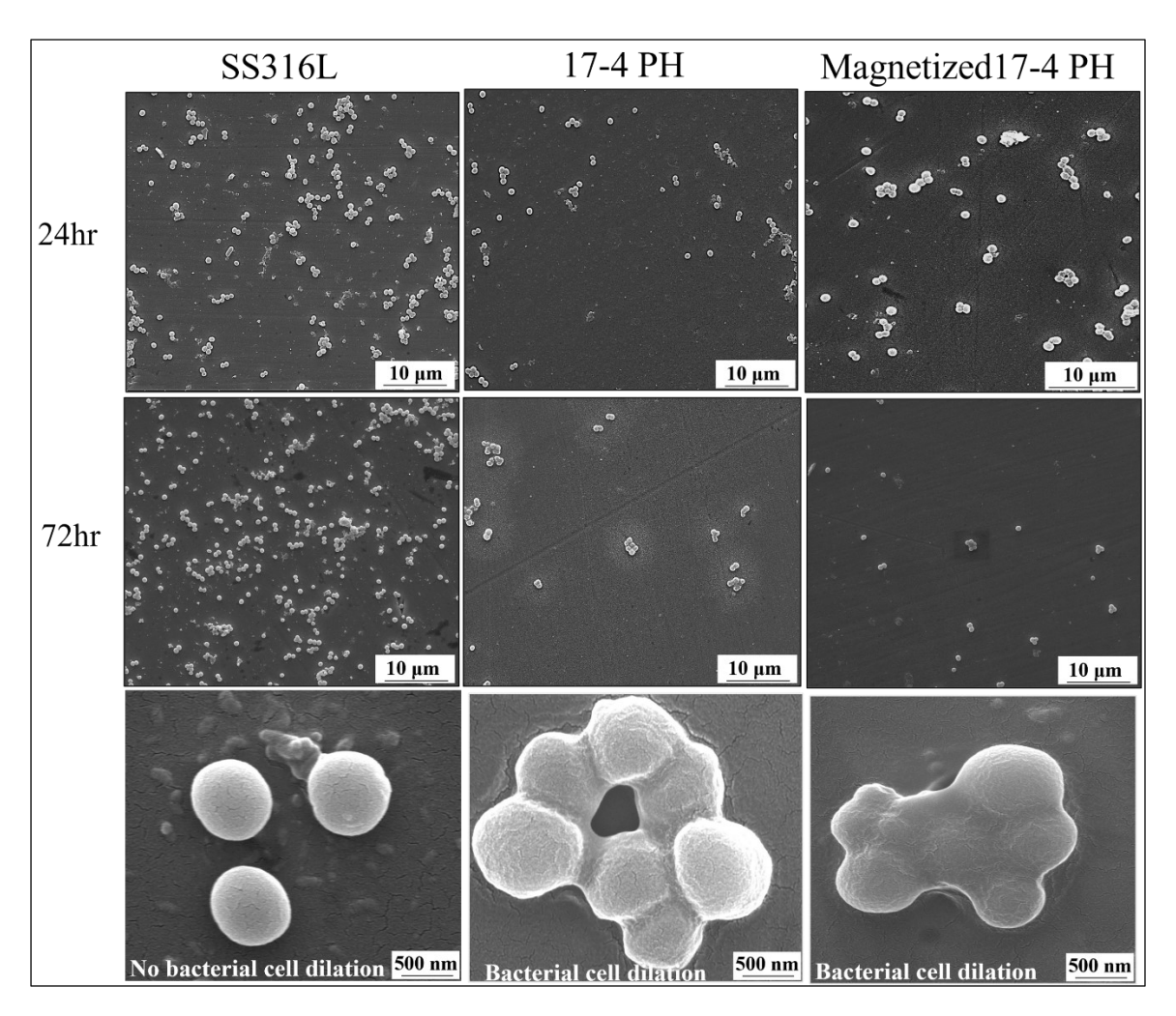


Figure 6: SEM micrographs showing the bacterial morphology of the *S. aureus* strain after 24 and 72 h culture. The surface of the SS316L control specimen showed increased bacterial proliferation from 24 to 72 h. Ultra-high magnification image of the control specimen showed the healthy morphology of the *S. aureus* bacterial strain. However, the surface of the 17- 4 PH and the Magnetized 17-4 PH treatment specimens showed reduced bacterial proliferation from 24 to 72 h. The ultra-high magnification image of the treatment specimens shows bacterial cell apoptosis, which could be attributed to the presence of the antibacterial agent copper.

3.5 In vitro gram-negative P. aeruginosa bacterial culture

To bolster the outcomes derived from the *in vitro* gram-positive bacterial culture, a secondary bacterial inhibition study involving a gram-negative bacterial strain, *P. aeruginosa*, was conducted. In contrast to the *S. aureus* bacterium, the *P. aeruginosa* strain necessitates a distinctive Pseudosel agar medium for culture. Pyoverdine (PVDI), a vital nutrient intrinsic to *P. aeruginosa*, exhibits a distinct bright green fluorescence under UV light exposure when cultured on a Pseudosel agar medium. This approach offers a comprehensive exploration of bacterial responses across different strains and further enriches the diversity of the experimental framework.

The quantitative representation of viable *P. aeruginosa* colonies for each composition is shown in **Fig. 7a**. 17-4 PH exhibited antibacterial efficacy, 54% and 70% against the *P. aeruginosa* strain after 24 and 72 h, respectively, **Fig. 7b**. Magnetized 17-4 PH showed antibacterial efficacy of 45% and 66% against the *P. aeruginosa* strain after 24 and 72 h, respectively, **Fig. 7b**. The morphological study of *P. aeruginosa* using SEM revealed an upsurge in bacterial growth on the surface of SS316L control specimens from 24 to 72 h. This augmentation was substantiated by SEM images showing the presence of robust and healthy bacterial colonies on the surface. In contrast, the treatment specimens, as-processed and magnetized 17-4 PH, exhibited a decline in bacterial growth over the same duration. **Fig. 8** shows SEM micrographs of the complete rupture of the bacterial cell membrane for as-processed and magnetized 17-4 PH within 72 h of exposure.

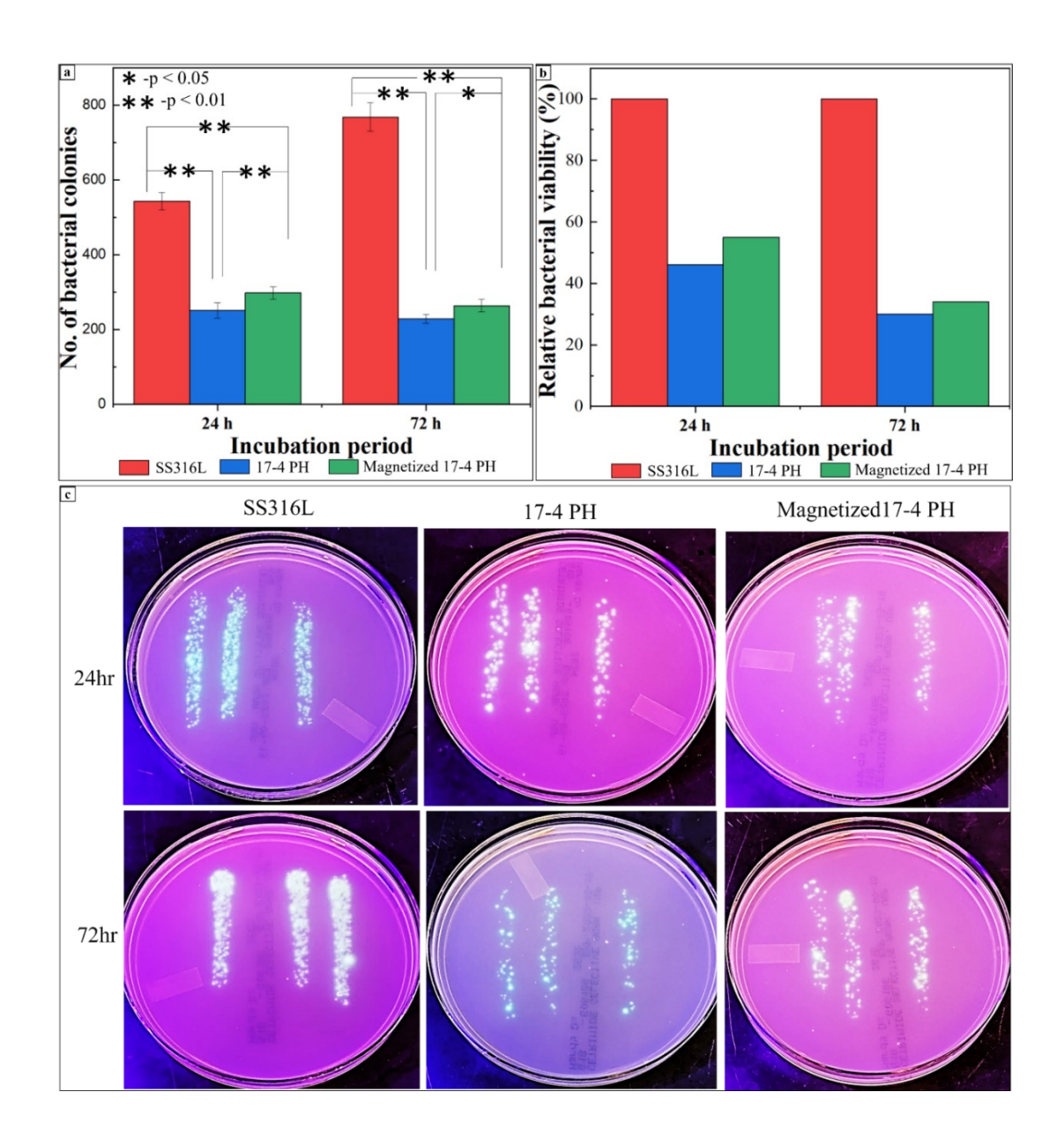


Figure 7: Results from the *in vitro* bacterial inhibition experiment against *P. aeruginosa*. (a) quantitative representation of the number of CFUs after 24 and 72 h culture of the *P. aeruginosa* bacterial strain. Statistical analyses were conducted using a one-way analysis of variance for a sample size (n) of 3 and a p-value of 0.05. Statistical significance was determined through pairwise assessment of means between control and treatments and among treatments. Results with p < 0.05 were considered significantly different and marked with '*', while those with p < 0.01 were regarded as extremely significant and denoted by '**'; (b) plot showing relative bacterial viability after 24 and 72 h culture, (c) high-definition agar plate images showing the CFU formation for *P. aeruginosa* for 24 and 72h.

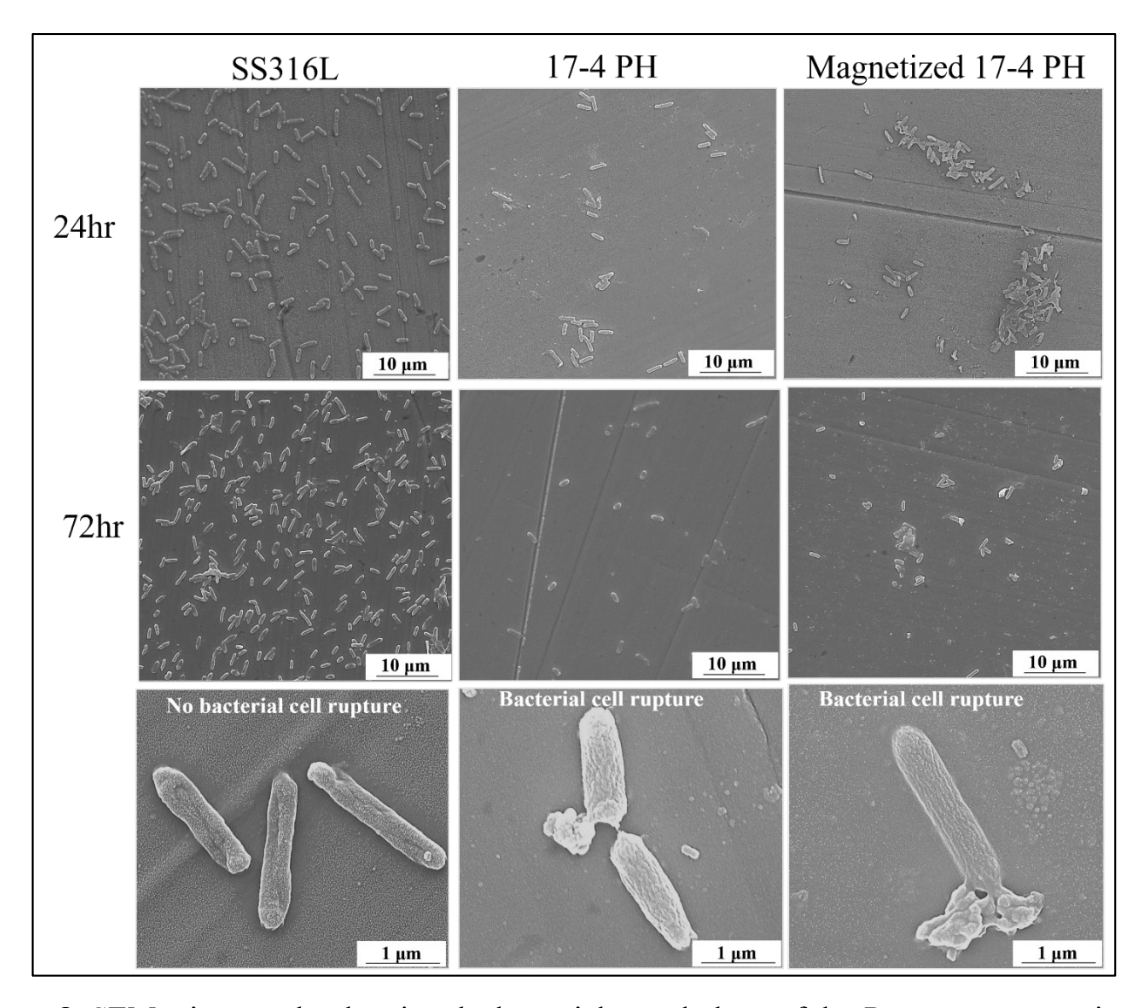


Figure 8: SEM micrographs showing the bacterial morphology of the *P. aeruginosa* strain after 24 and 72 h culture. The surface of the SS316L control specimen showed increased bacterial proliferation from 24 to 72 h. Ultra-high magnification image of the control specimen showed the healthy morphology of the *P. aeruginosa* bacterial strain. However, the surface of the 17-4 PH and the Magnetized 17-4 PH treatment specimens showed reduced bacterial proliferation from 24 to 72 h. The ultra-high magnification image of the treatment specimens shows bacterial cell apoptosis, which could be attributed to the presence of the antibacterial agent copper.

Both the bacterial strains showed a reduced bacterial colony count i.e., enhanced anti-bacterial property for the treatment samples 17-4 PH (T1) and magnetized 17-4 PH (T2) relative to control SS316L for the 24h and 72 h time points. This can be attributed to the presence of copper in T1 and T2. The release of copper from the surface of T1 and T2 successfully kills the

bacterial strains and inhibits further bacterial growth from 24h. to 72 h. The absence of copper in the control sample increases bacterial growth from 24h. to 72 h.

4 Discussion

Within the spectrum of stainless-steel grades, a selective fifteen find prevalent use across diverse commercial sectors [9]. Conforming to ASTM standard F899-23 [48], surgical applications gravitate toward austenitic (Class 3) and precipitation-hardened (Class 5) stainless steels among the commonly employed commercial grades [48]. SS316L, an ideal nonmagnetic austenitic stainless steel, has entrenched itself in numerous biomedical applications owing to its commercial availability and mechanical properties, particularly corrosion resistance [49]. From a pragmatic perspective, SS316L emerges as the material of choice in various biomedical applications, ranging from total arthroplasty to fracture fixations. However, designated as a 'firstgen biomaterial' [50], SS316L faces challenges, notably bacterial adhesion to its surface, osteomyelitis, and leading to implant failure. 17-4 PH emerges as a recognized precipitationhardened magnetic surgical stainless steel [48], distinguished by exceptional mechanical properties, intrinsic copper content, and reduced levels of metals like nickel. The presence of copper, known for its infection-prevention properties, holds promise for averting potential infections at the implant site. The ensuing discourse delves into a comprehensive exploration of the potential advantages of 17-4 PH stainless steel as a viable substitute for SS316L in some fracture management devices.

4.1 Microstructure, phase analysis, and mechanical properties

The SEM micrographs of the SS316L surfaces can be categorized into cellular (**Fig. 2a2**), columnar dendritic (**Fig. 2a3**), and dendritic (**Fig. 2a4**) microstructures. The primary reason for this inconsistency is the faster cooling and scanning direction of the energy source associated with the DED process [51]. The dynamic transformation of microstructure can be understood using the relationship between the rate of solidification growth (R) and the temperature gradient (G). The proportion of G to R is a critical determinant in understanding the morphology of the solidification microstructure. A higher value of G/R is the reason for cellular microstructure

(Fig. 2a₂), whereas a moderate value of G/R leads to a columnar dendritic (Fig. 2a₃) and slenderer dendritic (Fig. 2a₄) microstructure, respectively [35]. Unlike the SS316L, the SEM micrographs of the 17-4 PH surfaces exhibit a consistent lathy martensitic morphology. This microstructural homogeneity can be ascribed to a synergistic effect of the printing process, raw material used, and the chromium equivalent (Cr_{eq}) to nickel equivalent (Ni_{eq}) ratio. During printing 17-4 PH specimens, a delay time between consecutive layers was implemented to mitigate specimen overheating. This strategic delay resulted in accelerated and uniform cooling at each layer, ultimately yielding a homogeneous microstructure. It has also been reported that minor fluctuations in the chemical composition of the powder, particularly in the concentrations of ferrite and austenite stabilizers, exert a substantial influence on the phases in the as-printed samples. The Cr_{eq}/Ni_{eq} for the 17-4 PH specimen was calculated as 2.43, and according to previous research [35], [52], higher martensite transformation is observed when $Cr_{eq}/Ni_{eq} \sim 2.36$. The convergence of these three mechanisms is the underlying cause for the homogeneous lathy martensitic microstructure in 17-4 PH specimens.

The phase analysis results obtained from the XRD analysis are in line with the microstructure analysis. Only γ (FCC) and α (BCC) phases were observed on the SS316L and 17-4 PH specimens. However, both specimens demonstrate a positive peak shift and broadening compared to their powder counterparts. Peak broadening may occur due to repeated cycles of melting and solidification. However, the primary factors contributing to the shift in diffraction peaks will likely be residual stresses due to faster cooling. The SS316L showed a reducing trend for the hardness values from the first to the final layer, while the same was less pronounced for the 17-4 PH. This behavior is due to the variation in microstructural grain size between the final and initial layers of both specimens. It was found that the printed SS316L experienced a reduction in grain size by approximately 75% from the final layer to the initial layer, whereas the reduction for the 17-4 PH specimen was around 46%. The Hall-Petch equation shows an inverse relationship between grain size and mechanical properties. Given that the variation in grain size is more pronounced in the SS316L than in the 17-4 PH, the reduction in the trend of the hardness profile is more noticeable in the former [35].

The SS316L demonstrated an improved yield strength than conventionally manufactured samples, stemming from the enhanced dislocation density inherent to additively

manufactured materials [47]. This correlation adheres to Taylor-strengthening principles, conceptualizing the cells as an assembly of forest dislocations [53]. The SS316L specimen showed linear strain hardening in the plastic deformation zone, attributed to microstructural anisotropy arising from rapid cooling and solidification, inducing residual stresses. Upon phase and microstructural analyses, it was unveiled that the SS316L primarily comprises γ -phase with an FCC structure, exhibiting superior ductility. This is visibly demonstrated in the protruding edges of the post-compressed specimen. The insert Fig. 3b₂ shows the deformation behavior of the SS316L specimen. The 17-4 PH specimen demonstrated an increase of over 150% in the compressive yield strength compared to the SS316L. The martensitic structure of the 17–4 PH is known for its high dislocation density in both as-printed and solution-annealed states [54]. This mechanism accelerates the formation of nanometric Cu-rich precipitates [55], with sizes ranging from 10 to 20 nm under optimal aging conditions. These precipitates act as obstacles, impeding dislocation mobility through the Orowan mechanism and enhancing the compressive strength of the as-printed 17-4 PH specimens [56]. The post-compression sample's SEM micrograph in Fig. **3b**₁ shows numerous surface cracks attributed to the inherent brittleness of the samples [35]. The 17-4 PH specimen exhibits superior mechanical properties, necessitating its exploration in subsequent analyses of biological properties.

4.2 Effect of magnetization on hFOB proliferation

Static magnetic fields (SMFs) have been shown to modulate the proliferation, differentiation, and functionality of various bone cell types, including bone marrow mesenchymal stem cells (BMSCs), osteoblasts, bone marrow monocytes (BMMs), osteoclasts, and osteocytes [57]. In the current investigation, an average magnetic field intensity of 168±13 µT is generated in a batch of 17-4 PH specimens using an electromagnetic induction process, and hFOB cells were cultured on the top surfaces. After 3 days of culture, the magnetized 17-4 PH specimens showed 17% more OD value, and after 7 days, they showed a 25% increase over the SS316L control. Numerous studies have reported that the proliferation of OB cells was improved by applying a magnetic field [58], [59]. Another critical factor that regulates the proliferation of bone cells is the initial seeding density [60]. We have seeded 25 x 10³ hFOB cells per well. While the precise impact of SMFs on cellular development remains incompletely elucidated, the

mechanical transduction hypothesis is the most widely accepted explanation for SMFs' influence on cellular proliferation behavior [61]. SMFs stimulate both the cytoskeleton and cellular membrane, initiating a cascade of intracellular signals that culminate in the regulation of gene expression, thereby influencing cellular proliferation. The primary building blocks of orthopedic tissues comprise collagen fibers and hydroxyapatites, which are diamagnetic [62]. It was reported that the force exerted by the external magnetic field on the diamagnetic material is directly proportional to the intensity of magnetic induction and the gradient of the external magnetic field. Antimagnetic levitation [63], a phenomenon where the external magnetic field force is equal and opposite to the gravitational field force, is considered a crucial factor for the growth of osteoblasts [64]. Cellular and biological macromolecules, when exposed to a magnetic field, exhibit alignment either parallel or perpendicular to the field direction. Collagen aligns perpendicular to an applied external magnetic field, while OB cells without collagen align parallel to the field. Research indicates that the directional influence of magnetic fields could also enhance hFOB proliferation [65].

The interaction between SMFs and common bone growth factors promotes OB proliferation and growth. Multiple experiments have provided substantial evidence that SMFs enhance the production and expression of key growth factors such as 'transforming growth factor-β' (TGF-β1 [60], TGF-β3 [66]), 'leucine-rich transmembrane protein 3' (FLRT3) and 'BMP2' [67]. Moreover, these growth factors regulate OB proliferation through various signaling pathways, including canonical and noncanonical Mitogen-activated kinases (MAPKs) signaling pathways [68] involving p38, extracellular signal-regulated kinase (ERK), c-Jun N-terminal kinase (JNK), etc. [69]. Collectively, drawing on these references, it can be inferred that external magnetic fields can stimulate the proliferation and growth of OBs. Our research findings align with the existing literature and are schematically shown in **Fig 9**.

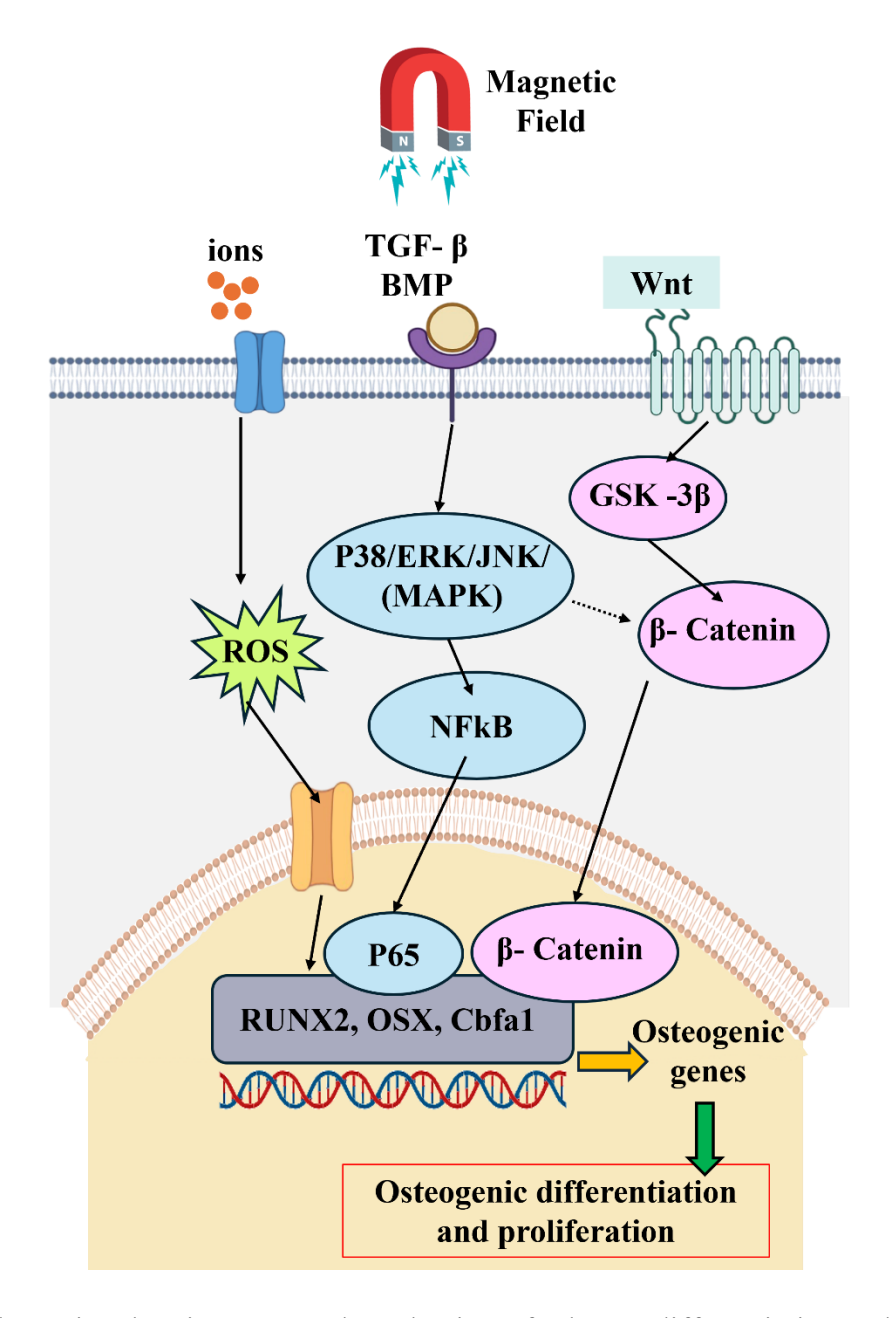


Figure 9: Schematics showing expected mechanisms for hFOB differentiation and proliferation due to the applied magnetic field.

While Cu plays a critical role as an essential trace element in biological systems, higher concentrations of ionic copper (Cu²⁺) can lead to cytotoxicity by generating excessive amounts of reactive oxygen species (ROS) through the Fenton and Haber-Weiss reactions [12], [70]. On the contrary, prior investigations have indicated that an optimal concentration of ionic Cu fosters

enhanced proliferation of OB cells and promotes superior cytocompatibility [71]. In the current study, the OD values of hFOB cells exhibited an upward trend on days 3 and 7. On day 3, the OD values of the as-processed and magnetized 17-4 PH specimens exhibited a 5% and 17% increase, respectively, compared to the SS316L control. Similarly, on day 7, the OD values of the as-processed and magnetized 17-4 PH specimens demonstrated a 7% and 25% increase to the SS316L control. These findings were statistically significant based on analysis of variance experiments. The non-cytotoxic behavior observed in the 17-4 PH specimens can be attributed to their enhanced corrosion resistance property, which ensures that the released ionic Cu from the specimen's surface remains within the bio-safety limit [72].

4.3 Effect of composition on bacterial inhibition

The historical documentation of copper's earliest medical utilization is found in the Smith Papyrus, one of the ancient manuscripts with enduring significance in the annals of medical literature [73]. Since then, Cu has been used globally as a bactericidal material. The bactericidal efficacy of Cu hinges on various influential factors, encompassing, yet not exhaustively, the physical state of Cu (nanoparticles or ions), the ionic form of Cu, the concentration of Cu interfacing with bacteria, the spatial vicinity of bacteria to surfaces comprising of Cu, the modality of application, such as wet or dry, etc. [12]. While the exact bactericidal mechanism of copper remains equivocal, the 'contact-killing' process is the most widely accepted theory. This process involves a series of events commencing with the dissolution of bacterial cell membranes due to the attack of Cu²⁺ ions. Subsequent steps include reducing membrane potential and cytoplasmic content, generating reactive oxygen species (ROS), and degrading bacterial DNA [73]. Further investigations have affirmed that the Cu²⁺ ions damage the respiratory enzymes and extract electrons from bacterial cell membranes, leading to membrane dissolution and cytoplasmic overflow and culminating in bacterial apoptosis [74]. The illustration showing the contact-killing process is given in Fig. 10.

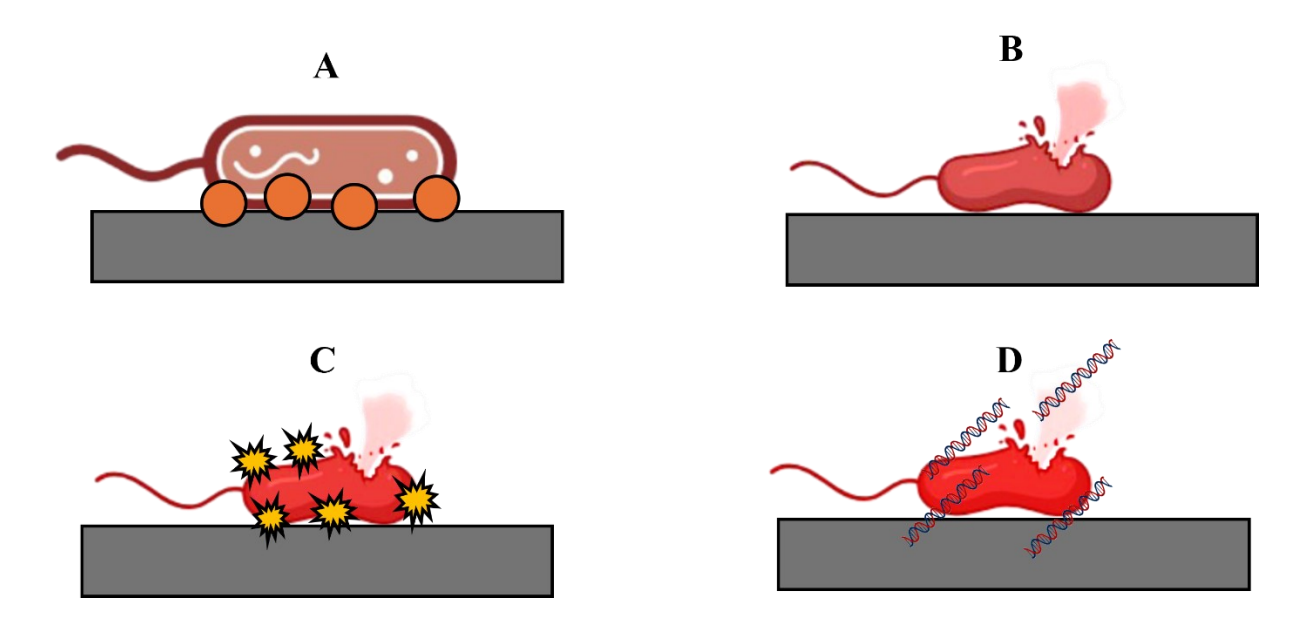


Figure 10: Illustrations showing the different events of contact killing of the bacteria on the 17-4 PH surface; (A) Copper ions dissolved from the 17-4 PH surface and attacking the bacterial cell surface, (B) The rupturing of the bacterial cell membrane due to the copper ions, leading to a reduction in membrane potential and cytoplasmic content, (C) generation of reactive oxygen species, (D) DNA degradation

Cu in the 17-4 PH demonstrated notable efficacy against *S. aureus* and *P. aeruginosa* strains. The 17-4 PH and the magnetized 17-4 PH specimens demonstrate bacterial efficacy as early as 24 h for both bacterial strains. Although the bacterial efficacy for *S. aureus* and *P. aeruginosa* on the magnetized 17-4 PH specimen was marginally lesser than that of the non-magnetized 17-4 PH, this difference did not reach extreme statistical significance. SEM images of the bacterial cell on as-processed and the magnetized 17-4 PH specimens revealed the cytoplasmic outflow and bacterial cell lysis after 24h of culture for both strains. These observations serve as morphological evidence indicating the bactericidal effect of copper.

5 Conclusions

SS316L and 17-4 PH samples were additively manufactured using the LDED process. The specimens were prepared and tested under three broad categories: metallurgical

characterization, mechanical characterization, and *in vitro* biological characterization. Key conclusions that can be drawn from this study are:

- Throughout the SS316L build, various microstructures, including cellular, columnar dendritic, and dendritic formations, were observed. However, 17-4 PH exhibited a consistent lathy martensite structure along its build. Phase analysis concurred with these microstructural findings, with SS316L displaying γ phases and 17-4 PH exhibiting martensitic α phase.
- The average microhardness of 17-4 PH surpassed that of SS316L by 48%. The compressive yield strength of 17-4 PH increased by over 150% compared to SS316L.
- Electromagnetic induction generated a static magnetic field in 17-4 PH specimens.
- The magnetized 17-4 PH specimens demonstrated 17% and 25% more optical density than SS316L specimens during *in vitro* hFOB cell culture.
- The 17-4 PH and magnetized 17-4 PH specimens demonstrated notable efficacy against *S. aureus* and *P. aeruginosa* bacterial strains as early as 24 h.

Considering these findings, it can be inferred that additively manufactured 17-4 PH possess notable significance to be used as a potential alternative to the SS316L in temporary fracture management devices, specifically locking and stabilization screws and pins designed to be removed within 1-2 years post-wound healing.

6 Acknowledgments

The authors would like to acknowledge financial support from the National Science Foundation under Grant Number CMMI 1934230 and the National Institute of Arthritis and Musculoskeletal and Skin Diseases of the National Institutes of Health under Award Number R01 AR078241 (PI—Bandyopadhyay). The content is solely the authors' responsibility and does not necessarily represent the National Institutes of Health's official views. The authors would also like to acknowledge financial support from the JCDREAM (Seattle, WA) to acquire critical research equipment used in this work.

7 Declaration of competing interest

The authors declare that they have no known competing financial interests or personal relationships that could have appeared to influence the work reported in this paper.

8 Data availability statement

The authors declare that all data supporting the findings of this study are available within the paper.

9 Reference

- [1] World Health Organization, "https://www.who.int/news-room/fact-sheets/detail/road-traffic-injuries." Accessed: Jan. 27, 2024. [Online]. Available: https://www.who.int/news-room/fact-sheets/detail/road-traffic-injuries
- [2] P. Devasconcellos, S. Bose, H. Beyenal, A. Bandyopadhyay, and L. G. Zirkle, "Antimicrobial particulate silver coatings on stainless steel implants for fracture management," *Materials Science and Engineering C*, vol. 32, no. 5, pp. 1112–1120, Jul. 2012, doi: 10.1016/j.msec.2012.02.020.
- [3] Z. Wu, B. Chan, J. Low, J. J. H. Chu, H. W. D. Hey, and A. Tay, "Microbial resistance to nanotechnologies: An important but understudied consideration using antimicrobial nanotechnologies in orthopaedic implants," Oct. 01, 2022, *KeAi Communications Co.* doi: 10.1016/j.bioactmat.2022.02.014.
- [4] T. J. de Villiers and S. R. Goldstein, "Bone health 2022: an update," 2022, *Taylor and Francis Ltd.* doi: 10.1080/13697137.2021.1965408.
- [5] A. M. Wu *et al.*, "Global, regional, and national burden of bone fractures in 204 countries and territories, 1990–2019: a systematic analysis from the Global Burden of Disease Study 2019," *Lancet Healthy Longev*, vol. 2, no. 9, pp. e580–e592, Sep. 2021, doi: 10.1016/S2666-7568(21)00172-0.
- [6] A. Abdelsalam, G. O. Wassif, W. S. Eldin, M. A. Abdel-Hamid, and S. I. Damaty, "Frequency and risk factors of musculoskeletal disorders among kitchen workers," *Journal of the Egyptian Public Health Association*, vol. 98, no. 1, Dec. 2023, doi: 10.1186/s42506-023-00128-6.

- [7] The Business research company, "https://www.thebusinessresearchcompany.com/report/implantable-biomaterials-global-market-report."
- [8] Q. Chen and G. A. Thouas, "Metallic implant biomaterials," 2015, *Elsevier Ltd.* doi: 10.1016/j.mser.2014.10.001.
- [9] A. Nouri and C. Wen, "Stainless steels in orthopedics," in *Structural Biomaterials: Properties, Characteristics, and Selection*, Elsevier, 2021, pp. 67–101. doi: 10.1016/B978-0-12-818831-6.00008-2.
- [10] Y. Zheng *et al.*, "Accelerated corrosion of 316L stainless steel in a simulated oral environment via extracellular electron transfer and acid metabolites of subgingival microbiota," *Bioact Mater*, vol. 35, pp. 56–66, May 2024, doi: 10.1016/j.bioactmat.2024.01.007.
- [11] Z. C. Lum, K. M. Natsuhara, T. J. Shelton, M. Giordani, G. C. Pereira, and J. P. Meehan, "Mortality During Total Knee Periprosthetic Joint Infection," *Journal of Arthroplasty*, vol. 33, no. 12, pp. 3783–3788, Dec. 2018, doi: 10.1016/j.arth.2018.08.021.
- [12] A. Bandyopadhyay *et al.*, "Additively manufactured Ti–Ta–Cu alloys for the next-generation load-bearing implants," *International Journal of Extreme Manufacturing*, vol. 6, no. 1, p. 015503, Feb. 2024, doi: 10.1088/2631-7990/ad07e7.
- [13] A. Muñoz and M. Costa, "Elucidating the mechanisms of nickel compound uptake: A review of particulate and nano-nickel endocytosis and toxicity," Apr. 01, 2012. doi: 10.1016/j.taap.2011.12.014.
- [14] R. L. Zondervan, J. J. Vaux, M. J. Blackmer, B. G. Brazier, and C. J. Taunt, "Improved outcomes in patients with positive metal sensitivity following revision total knee arthroplasty," *J Orthop Surg Res*, vol. 14, no. 1, Jun. 2019, doi: 10.1186/s13018-019-1228-4.
- [15] S. An, D. R. Eo, I. Sohn, and K. Choi, "Homogenization on solution treatment and its effects on the precipitation-hardening of selective laser melted 17-4PH stainless steel," *J Mater Sci Technol*, vol. 166, pp. 47–57, Dec. 2023, doi: 10.1016/j.jmst.2023.04.055.
- [16] S. Wang, K. Yang, M. Shen, and C. Yang, "Effect of Cu content on antibacterial activity of 17-4 PH stainless steel," *Materials Technology*, vol. 30, no. B2, pp. B115–B119, May 2015, doi: 10.1179/1753555714Y.0000000176.
- [17] I. T. Hong and C. H. Koo, "Antibacterial properties, corrosion resistance and mechanical properties of Cu-modified SUS 304 stainless steel," *Materials Science and Engineering: A*, vol. 393, no. 1–2, pp. 213–222, Feb. 2005, doi: 10.1016/j.msea.2004.10.032.
- [18] S. A. M. Tofail, E. P. Koumoulos, A. Bandyopadhyay, S. Bose, L. O'Donoghue, and C. Charitidis, "Additive manufacturing: scientific and technological challenges, market uptake and opportunities," Jan. 01, 2018, *Elsevier B.V.* doi: 10.1016/j.mattod.2017.07.001.

- [19] D. Svetlizky *et al.*, "Directed energy deposition (DED) additive manufacturing: Physical characteristics, defects, challenges and applications," Oct. 01, 2021, *Elsevier B.V.* doi: 10.1016/j.mattod.2021.03.020.
- [20] I. Mitra *et al.*, "3D Printing in alloy design to improve biocompatibility in metallic implants," *Materials Today*, vol. 45, pp. 20–34, May 2021, doi: 10.1016/j.mattod.2020.11.021.
- [21] F. A. España, V. K. Balla, S. Bose, and A. Bandyopadhyay, "Design and fabrication of CoCrMo alloy based novel structures for load bearing implants using laser engineered net shaping," *Materials Science and Engineering C*, vol. 30, no. 1, pp. 50–57, Jan. 2010, doi: 10.1016/j.msec.2009.08.006.
- [22] B. E. Carroll *et al.*, "Functionally graded material of 304L stainless steel and inconel 625 fabricated by directed energy deposition: Characterization and thermodynamic modeling," *Acta Mater*, vol. 108, pp. 46–54, Apr. 2016, doi: 10.1016/j.actamat.2016.02.019.
- [23] A. Bandyopadhyay, K. D. Traxel, M. Lang, M. Juhasz, N. Eliaz, and S. Bose, "Alloy design via additive manufacturing: Advantages, challenges, applications and perspectives," Jan. 01, 2022, *Elsevier B.V.* doi: 10.1016/j.mattod.2021.11.026.
- [24] A. Bandyopadhyay, Y. Zhang, and B. Onuike, "Additive manufacturing of bimetallic structures," 2022, *Taylor and Francis Ltd.* doi: 10.1080/17452759.2022.2040738.
- [25] F. Mcdonald, "Effect of Static Magnetic Fields on Osteoblasts and Fibroblasts In Vitro," 1993.
- [26] K. Marycz, K. Kornicka, and M. Röcken, "Static Magnetic Field (SMF) as a Regulator of Stem Cell Fate New Perspectives in Regenerative Medicine Arising from an Underestimated Tool," *Stem Cell Rev*, vol. 14, no. 6, p. 785, Dec. 2018, doi: 10.1007/S12015-018-9847-4.
- [27] T. P. Ribeiro, M. Flores, S. Madureira, F. Zanotto, F. J. Monteiro, and M. S. Laranjeira, "Magnetic Bone Tissue Engineering: Reviewing the Effects of Magnetic Stimulation on Bone Regeneration and Angiogenesis," Apr. 01, 2023, *Multidisciplinary Digital Publishing Institute (MDPI)*. doi: 10.3390/pharmaceutics15041045.
- [28] M. Marędziak, K. Marycz, D. Lewandowski, A. Siudzińska, and A. Śmieszek, "Static magnetic field enhances synthesis and secretion of membrane-derived microvesicles (MVs) rich in VEGF and BMP-2 in equine adipose-derived stromal cells (EqASCs)—a new approach in veterinary regenerative medicine," *In Vitro Cell Dev Biol Anim*, vol. 51, no. 3, p. 230, Mar. 2015, doi: 10.1007/S11626-014-9828-0.
- [29] E. Costantini *et al.*, "Improved osteogenic differentiation by extremely low electromagnetic field exposure: possible application for bone engineering," *Histochem Cell Biol*, vol. 158, no. 4, pp. 369–381, Oct. 2022, doi: 10.1007/s00418-022-02126-9.

- [30] J. Miyakoshi, "Effects of static magnetic fields at the cellular level," *Prog Biophys Mol Biol*, vol. 87, no. 2–3, pp. 213–223, Feb. 2005, doi: 10.1016/J.PBIOMOLBIO.2004.08.008.
- [31] M. A. Riley, A. D. Walmsley, and I. R. Harris, "Magnets in prosthetic dentistry," *J Prosthet Dent*, vol. 86, no. 2, pp. 137–142, 2001, doi: 10.1067/MPR.2001.115533.
- [32] A. Rutkovskiy, K.-O. Stensløkken, and I. J. Vaage, "Osteoblast Differentiation at a Glance," *Med Sci Monit Basic Res*, vol. 22, pp. 95–106, Sep. 2016, doi: 10.12659/msmbr.901142.
- [33] M. A. Darendeliler, A. Darendeliler, and P. M. Sinclair, "Effects of static magnetic and pulsed electromagnetic fields on bone healing.," *Int J Adult Orthodon Orthognath Surg*, vol. 12, no. 1, pp. 43–53, Jan. 1997, Accessed: Feb. 21, 2023. [Online]. Available: https://europepmc.org/article/med/9456617
- [34] C. Xu, Z. Fan, Y. L. Chao, L. Du, and F. Q. Zhang, "Magnetic fields of 10mT and 120mT change cell shape and structure of F-actins of periodontal ligament cells," *Bioelectrochemistry*, vol. 72, no. 1, pp. 41–46, Feb. 2008, doi: 10.1016/J.BIOELECHEM.2007.11.009.
- [35] A. Dash and A. Bandyopadhyay, "17-4 PH and SS316L bimetallic structures via additive manufacturing," *Virtual Phys Prototyp*, vol. 19, no. 1, 2024, doi: 10.1080/17452759.2023.2292695.
- [36] Jr.; D. K.; I. G.; A. B. David L. Bourell; Joseph J. Beaman, "Rapid Prototyping," in *Composites, ASM Hand Book*, 1st ed., vol. 21, Daniel B. Miracle and Steven L. Donaldson, Eds., ASM, 2001, pp. 383–387.
- [37] ASTM E407-07, "Designation: E407 07 (Reapproved 2015) '1 Standard Practice for Microetching Metals and Alloys 1," *ASTM International*, 2015, doi: 10.1520/E0407-07R15E01.
- [38] ASTM E92-23, "Standard Test Methods for Vickers Hardness and Knoop Hardness of Metallic Materials 1 Verification of Vickers and Knoop Hardness Testing Machines Annex A1 Vickers and Knoop Hardness Standardizing Machines Annex A2 Standardization of Vickers and Knoop Indenters Annex A3 Standardization of Vickers and Knoop Hardness Test Blocks Annex A4 Correction Factors for Vickers Hardness Tests Made on Spherical and Cylindrical Surfaces Annex A5", doi: 10.1520/E0092-23.
- [39] ASTM E9-19, "Standard Test Methods of Compression Testing of Metallic Materials at Room Temperature 1," *ASTM International*, doi: 10.1520/E0009-19.
- [40] V. K. Balla, S. Bodhak, S. Bose, and A. Bandyopadhyay, "Porous tantalum structures for bone implants: Fabrication, mechanical and in vitro biological properties," *Acta Biomater*, vol. 6, no. 8, pp. 3349–3359, 2010, doi: 10.1016/j.actbio.2010.01.046.

- [41] S. Bodhak *et al.*, "In vitro biological and tribological properties of transparent magnesium aluminate (Spinel) and aluminum oxynitride (ALON®)," *Journal of Materials Science: Materials in Medicine 2011 22:6*, vol. 22, no. 6, pp. 1511–1519, May 2011, doi: 10.1007/S10856-011-4332-5.
- [42] C. Wiegand *et al.*, "Critical physiological factors influencing the outcome of antimicrobial testing according to ISO 22196 / JIS Z 2801," *PLoS One*, vol. 13, no. 3, Mar. 2018, doi: 10.1371/journal.pone.0194339.
- [43] A. Dash, L. Squires, J. D. Avila, S. Bose, and A. Bandyopadhyay, "Influence of active cooling on microstructure and mechanical properties of wire arc additively manufactured mild steel," *Front Mech Eng*, vol. 9, 2023, doi: 10.3389/fmech.2023.1130407.
- [44] A. Bandyopadhyay *et al.*, "Wire-arc directed energy deposition of monolithic and bimetallic structures of maraging 250 steel," *Virtual Phys Prototyp*, vol. 19, no. 1, 2024, doi: 10.1080/17452759.2023.2296127.
- [45] H. R. Lashgari, C. Kong, E. Adabifiroozjaei, and S. Li, "Microstructure, post thermal treatment response, and tribological properties of 3D printed 17-4 PH stainless steel," *Wear*, vol. 456–457, Sep. 2020, doi: 10.1016/j.wear.2020.203367.
- [46] A693 22, "Standard Specification for Precipitation-Hardening Stainless and Heat-Resisting Steel Plate, Sheet, and Strip 1," *ASTM International*, doi: 10.1520/A0693-22.
- [47] ASTM SA240, "SPECIFICATION FOR CHROMIUM AND CHROMIUM-NICKEL STAINLESS STEEL PLATE, SHEET, AND STRIP FOR PRESSURE VESSELS AND FOR GENERAL APPLICATIONS," ASTM International, 2007.
- [48] ASTM F899-23, "Standard Specification for Wrought Stainless Steels for Surgical Instruments 1", doi: 10.1520/F0899-23.
- [49] M. Navarro, A. Michiardi, O. Castaño, and J. A. Planell, "Biomaterials in orthopaedics," Oct. 06, 2008, *Royal Society*. doi: 10.1098/rsif.2008.0151.
- [50] L. L. Hench, "Biomaterials," *Science* (1979), vol. 208, no. 4446, pp. 826–831, May 1980, doi: 10.1126/science.6246576.
- [51] J. T. Pacheco *et al.*, "Laser directed energy deposition of AISI 316L stainless steel: The effect of build direction on mechanical properties in as-built and heat-treated conditions," *Advances in Industrial and Manufacturing Engineering*, vol. 4, May 2022, doi: 10.1016/j.aime.2022.100079.
- [52] S. Vunnam, A. Saboo, C. Sudbrack, and T. L. Starr, "Effect of powder chemical composition on the as-built microstructure of 17-4 PH stainless steel processed by selective laser melting," *Addit Manuf*, vol. 30, Dec. 2019, doi: 10.1016/j.addma.2019.100876.
- [53] M. Shamsujjoha, S. R. Agnew, J. M. Fitz-Gerald, W. R. Moore, and T. A. Newman, "High Strength and Ductility of Additively Manufactured 316L Stainless Steel

- Explained," *Metall Mater Trans A Phys Metall Mater Sci*, vol. 49, no. 7, pp. 3011–3027, Jul. 2018, doi: 10.1007/s11661-018-4607-2.
- [54] L. Wang, C. Dong, C. Man, D. Kong, K. Xiao, and X. Li, "Enhancing the corrosion resistance of selective laser melted 15-5PH martensite stainless steel via heat treatment," *Corros Sci*, vol. 166, Apr. 2020, doi: 10.1016/j.corsci.2019.108427.
- [55] S. Sabooni *et al.*, "Laser powder bed fusion of 17–4 PH stainless steel: A comparative study on the effect of heat treatment on the microstructure evolution and mechanical properties," *Addit Manuf*, vol. 46, p. 102176, Oct. 2021, doi: 10.1016/j.addma.2021.102176.
- [56] J. B. Ferguson *et al.*, "On the superposition of strengthening mechanisms in dispersion strengthened alloys and metal-matrix nanocomposites: Considerations of stress and energy," *Metals and Materials International*, vol. 20, no. 2, pp. 375–388, 2014, doi: 10.1007/s12540-014-2017-6.
- [57] J. Yang, Y. Feng, Q. Li, and Y. Zeng, "Evidence of the static magnetic field effects on bone-related diseases and bone cells," Jan. 01, 2023, *Elsevier Ltd.* doi: 10.1016/j.pbiomolbio.2022.11.006.
- [58] E. C. Kim, J. Park, I. K. Kwon, S. W. Lee, S. J. Park, and S. J. Ahn, "Static magnetic fields promote osteoblastic/cementoblastic differentiation in osteoblasts, cementoblasts, and periodontal ligament cells," *J Periodontal Implant Sci*, vol. 47, no. 5, pp. 273–291, Oct. 2017, doi: 10.5051/jpis.2017.47.5.273.
- [59] J. Na *et al.*, "Static magnetic field regulates proliferation, migration, and differentiation of human dental pulp stem cells by MAPK pathway," *Cytotechnology*, vol. 74, no. 3, pp. 395–405, Jun. 2022, doi: 10.1007/s10616-022-00533-3.
- [60] H. M. Huang, S. Y. Lee, W. C. Yao, C. T. Lin, and C. Y. Yeh, "Static magnetic fields upregulate osteoblast maturity by affecting local differentiation factors," *Clin Orthop Relat Res*, vol. 447, pp. 201–208, 2006, doi: 10.1097/01.blo.0000203464.35561.be.
- [61] W. W. C. Albuquerque, R. M. P. B. Costa, T. de Salazar e Fernandes, and A. L. F. Porto, "Evidences of the static magnetic field influence on cellular systems," May 01, 2016, *Elsevier Ltd.* doi: 10.1016/j.pbiomolbio.2016.03.003.
- [62] M. Nakayama *et al.*, "Stimuli-responsive hydroxyapatite liquid crystal with macroscopically controllable ordering and magneto-optical functions," *Nat Commun*, vol. 9, no. 1, Dec. 2018, doi: 10.1038/s41467-018-02932-7.
- [63] M. D. Simon and A. K. Geim, "Diamagnetic levitation: Flying frogs and floating magnets (invited)," *J Appl Phys*, vol. 87, no. 9 III, pp. 6200–6204, May 2000, doi: 10.1063/1.372654.

- [64] Y. L. Sun *et al.*, "Diamagnetic levitation promotes osteoclast differentiation from RAW264.7 cells," *IEEE Trans Biomed Eng*, vol. 62, no. 3, pp. 900–908, Mar. 2015, doi: 10.1109/TBME.2014.2370039.
- [65] H. Kotani *et al.*, "Strong static magnetic field stimulates bone formation to a definite orientation in vitro and in vivo," *Journal of Bone and Mineral Research*, vol. 17, no. 10, pp. 1814–1821, Oct. 2002, doi: 10.1359/jbmr.2002.17.10.1814.
- [66] H. D. Amin, M. A. Brady, J. P. St-Pierre, M. M. Stevens, D. R. Overby, and C. R. Ethier, "Stimulation of chondrogenic differentiation of adult human bone marrow-derived stromal cells by a moderate-strength static magnetic field," *Tissue Eng Part A*, vol. 20, no. 11–12, pp. 1612–1620, Jun. 2014, doi: 10.1089/ten.tea.2013.0307.
- [67] W. Li, S. Zhao, W. He, M. Zhang, S. Li, and Y. Xu, "Static magnetic fields accelerate osteogenesis by regulating FLRT/BMP pathway," *Biochem Biophys Res Commun*, vol. 527, no. 1, pp. 83–89, Jun. 2020, doi: 10.1016/j.bbrc.2020.04.090.
- [68] M. Wu, G. Chen, and Y. P. Li, "TGF-β and BMP signaling in osteoblast, skeletal development, and bone formation, homeostasis and disease," *Bone Res*, vol. 4, Apr. 2016, doi: 10.1038/boneres.2016.9.
- [69] E. Rodríguez-Carballo, B. Gámez, and F. Ventura, "p38 MAPK signaling in osteoblast differentiation," May 06, 2016, *Frontiers Media S.A.* doi: 10.3389/fcell.2016.00040.
- [70] M. E. Letelier, S. Sánchez-Jofré, L. Peredo-Silva, J. Cortés-Troncoso, and P. Aracena-Parks, "Mechanisms underlying iron and copper ions toxicity in biological systems: Prooxidant activity and protein-binding effects," *Chem Biol Interact*, vol. 188, no. 1, pp. 220–227, Oct. 2010, doi: 10.1016/j.cbi.2010.06.013.
- [71] J. Pablo Rodrguez, S. Ros, and M. Gonzlez, "Modulation of the proliferation and differentiation of human mesenchymal stem cells by copper," *J Cell Biochem*, vol. 85, no. 1, pp. 92–100, 2002, doi: 10.1002/jcb.10111.
- [72] Y. Yuan *et al.*, "Osteogenesis stimulation by copper-containing 316L stainless steel via activation of akt cell signaling pathway and Runx2 upregulation," *J Mater Sci Technol*, vol. 35, no. 11, pp. 2727–2733, Nov. 2019, doi: 10.1016/j.imst.2019.04.028.
- [73] G. Grass, C. Rensing, and M. Solioz, "Metallic copper as an antimicrobial surface," Mar. 2011. doi: 10.1128/AEM.02766-10.
- [74] J. P. Ruparelia, A. K. Chatterjee, S. P. Duttagupta, and S. Mukherji, "Strain specificity in antimicrobial activity of silver and copper nanoparticles," *Acta Biomater*, vol. 4, no. 3, pp. 707–716, 2008, doi: 10.1016/j.actbio.2007.11.006.

Supplemental Information

Tables

ST 1: Powder characteristics for SS3116L and 17-PH.

Composition	SS316L	17-4 PH			
		Min (%)	Max (%)		
Fe	Balance	Balance			
Cr	17	15.00	17.50		
Ni	12	3.00	5.00		
Mn	1.5	1			
Si	0.8	1			
Мо	2.5	0.50			
С	0.01	0.07			
Cu	Nil	3.00	5.00		
Nb+Ta	Nil	0.15	0.45		
О	0.06	0.040			
Al	Nil	0.050			
P	Nil	0.040			
N	Nil	0.0	0.030		
S	Nil	0.030			
Sn	Nil	0.020			

Figures

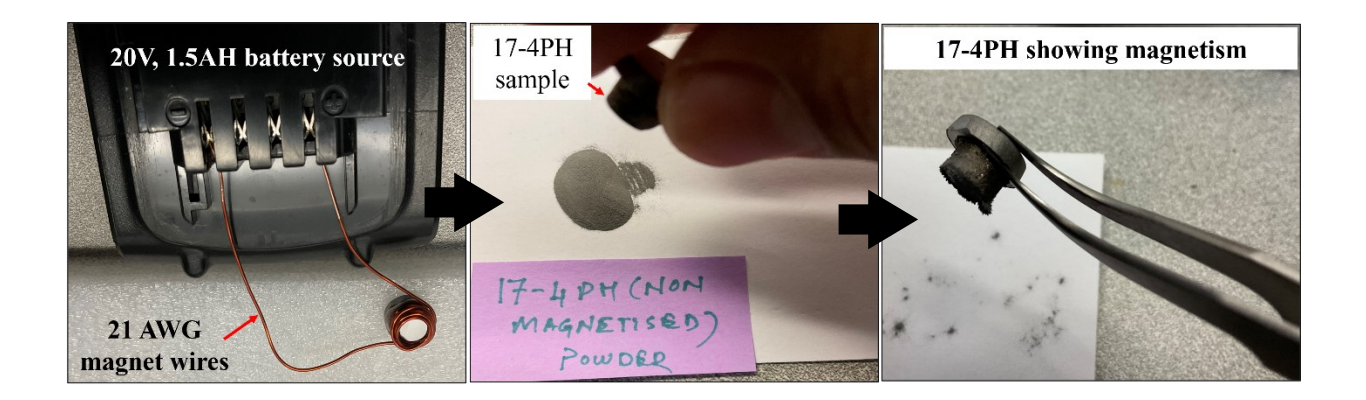


Figure S1: Magnetizing the additively manufactured 17-4 PH samples via electromagnetic induction process.

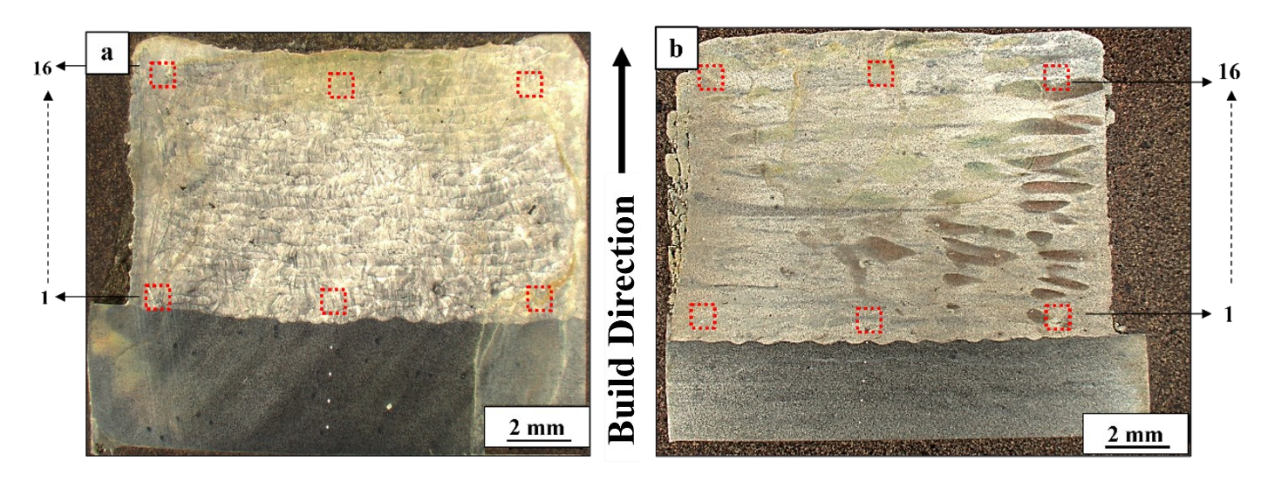


Figure S2: Hardness profile of (a) SS316L, (b) 17-4 PH with scanning direction along the build direction.